Xia et al. Journal of Nanobiotechnology (2025) 23:167
https://doi.org/10.1186/s12951-025-03255-8

Journal of Nanobiotechnology

RESEARCH Open Access

Cascade-recharged macrophage-biomimetic ruthenium-based nanobattery for enhanced photodynamic-induced immunotherapy

Guoyu Xia[1,2†], Zhongxiong Fan[1*†], Qingluo Wang[1,2], Jianmin Li[1,2], Yuxiang Zhang[5], Adila Aipire[2], Qiurong Su[3], Ying Li[3*], Zhenqing Hou[1,4*] and Jinyao Li[2*]

Abstract

Photodynamic-induced immunotherapy (PDI) is often hampered by low reactive oxygen species (ROS) yield, intratumor hypoxia, high glutathione (GSH) concentration, and immunosuppressive microenvironment. In view of this, a ruthenium (Ru)-based nanobattery (termed as IRD) with cascade-charged oxygen (O_2), ROS, and photodynamic-induced immunotherapy by coordination-driven self-assembly of transition-metal Ru, photosensitizer indocyanine green (ICG), and organic ligand dithiobispropionic acid (DTPA). Then, IRD is camouflaged with macrophage membranes to obtain a nanobattery (termed as IRD@M) with targeting and immune evasion capabilities. Upon intravenous administration, IRD@M with a core-shell structure, nano diameter, and good stability can specifically hoard in tumor location and internalize into tumor cells. Upon disassembly triggered by GSH, the released Ru^{3+} not only catalyzes the conversion of endogenous hydrogen peroxide (H_2O_2) into O_2 to alleviate tumor hypoxia and reduce the expression of hypoxia-inducible factor-1*α* (HIF-1*α*), but also generates hydroxyl radicals (·OH) to elevate intracellular ROS levels. This process significantly enhances the photodynamic therapy (PDT) efficacy of the released ICG. Meanwhile, the released DTPA can significantly downregulate overexpressed GSH to reduce the elimination of ROS deriving from PDT by the exchange reaction of thiol-disulfide bond. It is also found that alleviating the hypoxic tumor microenvironment synergistically enhances the PDT efficacy, which in turn cascades to recharge the subsequent immune response, significantly improving the immunosuppressive tumor microenvironment and activating systemic tumor-specific immunity. Notably, in vitro and in vivo experimental results jointly confirm that such cascade-recharged macrophage-biomimetic Ru-based nanobattery IRD@M can achieve an obvious tumor elimination while results in a minimized side effect. Taken together, this work highlights a promising strategy for simple, flexible, and effective Ru-based immunogenic cell death (ICD) agents within PDI.

†Guoyu Xia and Zhongxiong Fan contributed equally to this work.

*Correspondence:
Zhongxiong Fan
fanzhongxiong@xju.edu.cn
Ying Li
yinn.lee@163.com
Zhenqing Hou
houzhenqing@xmu.edu.cn
Jinyao Li
ljyxju@xju.edu.cn

Full list of author information is available at the end of the article

Graphical Abstract

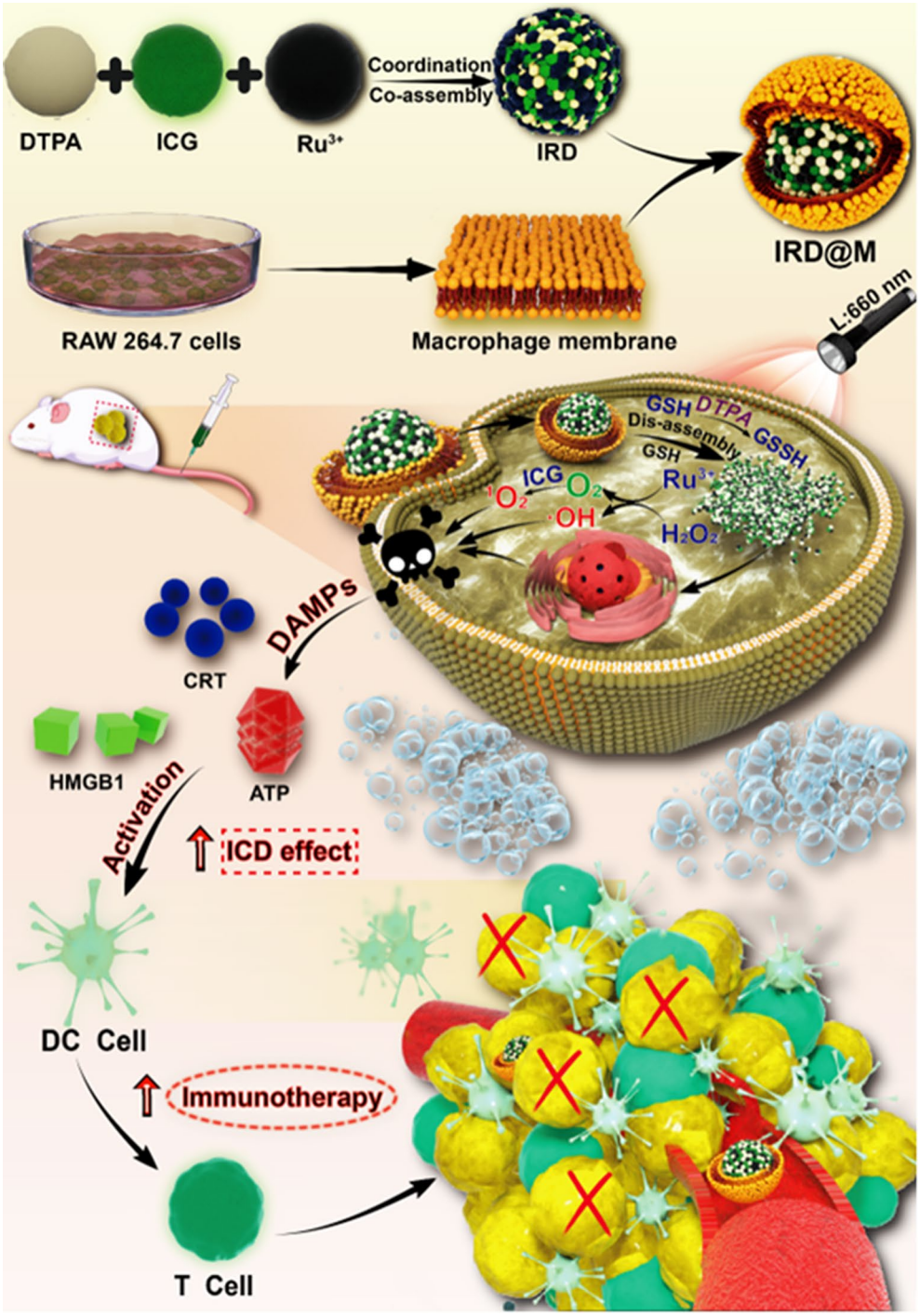

Keywords Macrophage membrane, Ruthenium, Photodynamic immunotherapy, Hypoxia, Tumor therapy

Introduction

In recent years, PDI has shown tremendous potential in cancer immunology due to its ability to safely and effectively trigger immune responses in the body [1, 2]. PDI is a sophisticated process that rapidly stimulates the production of ROS to directly kill cancer cells, induce ICD in tumor cells, expose tumor-associated antigens, release damage-associated factors, and trigger a cascade

of immune responses at the tumor site, while simultaneously promoting the infiltration of immune cells to eliminate tumor cells, optimizing the tumor immune microenvironment, and activating the body's immune system [3–6]. However, the hypoxic microenvironment created by the unique Warburg effect of tumor cells, combined with the aggregation-caused quenching (ACQ) effect of traditional photosensitizers and their low ROS yield, not only limits the efficacy of PDT itself but also impairs the activation and proliferation of various immune cells during PDI process, consequently affecting the initiation of different immune signaling pathways [7–11]. Therefore, how to rescue the sparse oxygen supply at the tumor site while improving the ACQ effect of photosensitizers and increasing the efficiency of ROS generation to cause a more potent ICD effect to reverse the immunosuppressed microenvironment is an important node in the PDI landscape.

Up to now, transition metal complexes (Ru, Ir, Pt) have been recognized as very promising PSs for PDT due to their highly efficient intersystemic scrambling (ISC) process, large Stokes shift, and tunable ligand structure, which endowed them with unique physical and biological properties conducive to the solution of the problems such as the ACQ phenomenon and the low ROS yield [12–17]. Among them, ruthenium, with its highly efficient catalytic properties and multispecies enzyme activities, has received growing attention. Thanks to its abundant d-electron orbitals and active valence electron interaction, ruthenium has been shown to possess catalase-like (CAT), peroxidase-like (POD), glucose oxidase-like, oxidase-like, nitric oxide synthase-like, and superoxide dismutase-like activities [18–22]. Therefore, effectively leveraging the unique properties of ruthenium metal presents an excellent strategy for addressing the challenges in PDI. However, high GSH concentrations in tumor cells may inactivate metal cofactors leading to diminished catalytic efficacy, while GSH as a scavenger of ROS halves the efficacy of PDT [23, 24]. Therefore, the introduction of organic ligands capable of depleting GSH is important to protect the catalytic activity of the metal as well as the efficacy of PDT. DTPA is an organic compound containing disulfide bonds that can react with the thiol groups in GSH, thereby reducing GSH levels and further enhancing PDI [25, 26]. However, traditional nanoparticle delivery strategies face significant limitations in penetrating dense tumor tissues and mitigating potential toxicity from off-target effects. Therefore, there is an urgent need for an advanced delivery system that can act as a bridge in PDI, addressing the shortcomings of existing delivery strategies.

Currently, biomimetic delivery systems derived from immune cell membranes have shown great promise in drug delivery applications. This is largely due to the complex receptor mechanisms on the cell membrane surface, which play a key role in intercellular communication and enable specific targeting of disease sites [27–29]. Particularly, as a key component of immune cells, macrophages possess several characteristics, including morphological flexibility, a rich array of surface receptors, low immunogenicity, and prolonged circulation time [30]. Additionally, the presence of self-marking molecules CD47 and CD45 enables macrophages to evade clearance by the mononuclear phagocyte system in vivo. Furthermore, these cells can effectively navigate to sites of inflammation and tumors by binding to specific proteins on their membrane surface, such as cell adhesion molecules and chemokine receptors, which interact with inflammatory chemokines at the lesion sites [31–33]. Therefore, combining the excellent biological properties of macrophage membranes with artificially manufactured nanocores endows the system with immune evasion characteristics, enhanced biocompatibility, and efficient navigation to inflammatory sites, making it highly promising in the PDI landscape.

Building on these insights, we designed a macrophage membrane-coated ruthenium-based nanobattery with the aim of enhancing PDT anti-cancer efficacy and potentially improving immune response. The macrophage membrane confers excellent targeting ability and immune evasion, facilitating the delivery of the nanomedicine to tumor sites. Once at the tumor site, Ru can continuously generate O_2 by catalyzing the high expression of H_2O_2, which supports PDT recharging and helps alleviate the hypoxic microenvironment, thus reducing the expression of HIF-1α. This improvement creates a more favorable environment for immune cell infiltration and activation. Additionally, the increased production of singlet oxygen ($^1O_2$) from IRD@M and the POD-like enzyme activity of Ru contribute to the generation of ·OH, which further enhances intracellular ROS levels in tumor cells. DTPA also disrupts the reductive system within tumor cells, helping to alleviate factors that limit ROS production and potentially altering the redox balance within the tumor cells. Finally, laser irradiation triggers the exposure of tumor-associated antigens and the release of damage-associated molecular patterns, which may recruit more immune cells to the tumor microenvironment and contribute to a positive feedback loop, potentially enhancing immune efficacy and tumor suppression (Scheme 1). In general, this strategy aims to address some of the limitations of conventional PDT, with the potential to enhance anti-tumor efficacy. Moreover, IRD@M may help modulate the tumor immune microenvironment, potentially reversing the "immune desert" and thereby improving the overall effectiveness of PDT.

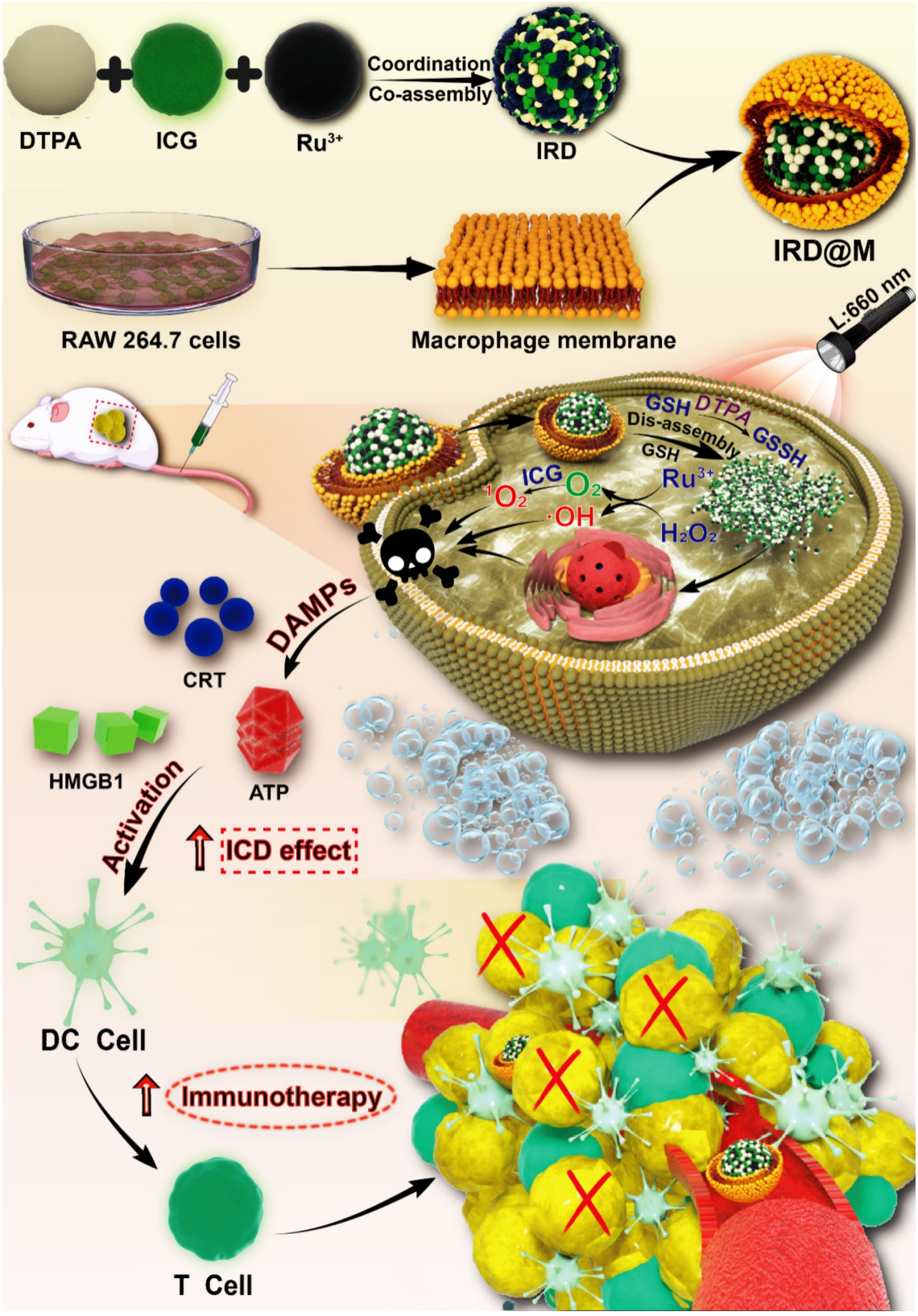

Scheme 1 The schematic illustrates the fabrication process and therapeutic strategy of IRD@M nanobattery. After intravenous injection, IRD@M precisely targets tumor sites, cascade-recharges O_2 and ROS levels, depletes intracellular GSH, effectively stimulating ICD effects induced by PDT, alleviating the hypoxic tumor microenvironment, recruiting more immune cells to infiltrate the tumor, and establishing a positive feedback loop of tumor immunotherapy, fully activating the potential of PDI

Results and discussion

Construction and characterization of IRD and IRD@M

Inspired by the excellent ROS production, fascinating enzyme-like activity, and good biocompatibility of ruthenium metal, we constructed a self-oxygen-supplying, ROS-generating nanobattery (named IRD) through coordinated self-assembly of Ru^{3+} metal ion, FDA-approved small molecule photosensitizer ICG, and the disulfide-rich organic compound DTPA. Firstly, we investigated its morphology using transmission electron microscopy (TEM). The TEM images showed that IRD exhibited uniform, regularly spherical shapes with good dispersion and intact structure, with a particle size of approximately 180 nm (Fig. 1A). Meanwhile, SEM also confirmed that IRD exhibits a uniform spherical morphology (Figure S1). Furthermore, to confirm successful integration of the three constituents into the IRD matrix, energy dispersive X-ray spectroscopy (EDS) was employed. Elemental mapping images demonstrated the presence of Ru, S, C, N, and O elements uniformly distributed within the IRD matrix (Fig. 1B).

Subsequently, to enhance the in vivo targeting capability of IRD and avoid immune system recognition, we coated the extracted macrophage membrane onto the surface of the IRD nanobattery through sonication, forming biomimetic nanobatteries encapsulated by the macrophage membrane. Firstly, the sample was subjected to ultrasonic treatment for 75 s, and its morphology was observed. No distinct and complete membrane coating was evident (Figure S2). Next, the sample was treated for 150 s, and TEM observation revealed the formation of a membrane approximately 31 nm thick around the particles. After coating, the particle size increased to around 213 nm, confirming the successful formation of the membrane coating (Fig. 1C). Additionally, dynamic light scattering (DLS) assessed the hydrodynamic size and surface charge of IRD and IRD@M. The analysis showed that IRD had a diameter of approximately 179.1 ± 2.6 nm with a polydispersity index of 0.16 ± 0.01, while IRD@M had a diameter of approximately 219 ± 1.0 nm with a PDI of 0.09 ± 0.02. These size data were consistent with TEM images, and the zeta potentials of IRD and IRD@M were measured as -24.4 mV and − 32.3 mV, respectively (Fig. 1D-E).Furthermore, SDS-PAGE analysis confirmed the successful membrane coating by demonstrating extremely similar protein bands between macrophage membrane and IRD@M before and after coating, as shown in Fig. 1F. Taken together, these results (increase in particle size, change in zeta potential, similar protein bands) collectively confirm the successful preparation of IRD@M.

Next, we firstly observed the crystalline shape of IRD by X-ray diffraction (XRD), as shown in Fig. 2A, the sharp crystalline diffraction peak of DTPA exists, and extensive amorphous diffraction peaks exist for ICG and $RuCl_3$, whereas the crystalline peaks of DTPA disappeared in IRD, and the characteristic amorphous peaks appeared instead, which may be due to the surface effect and the size effect at the nanometer scale of IRD, which leads to the obstruction of crystal formation and thus contributes to the formation of amorphous material. Then, Fourier Transform Infrared Spectroscopy (FTIR) was used to analyze the changes of functional groups in IRD. As illustrated in Fig. 2B, the characteristic peaks in ICG were shifted to higher wavelengths in IRD (1504 cm^{-1} and 1535 cm^{-1}), which may be due to the changes of the benzene ring skeleton [34]. Furthermore, it can be observed that the carbon-sulfur (C-S) bond at 941 cm^{-1} in DTPA is significantly attenuated in IRD, with no new characteristic peaks emerging. Subsequently, X-ray photoelectron spectroscopy (XPS) was employed to analyze the chemical composition and states on the surface of IRD. The XPS survey spectrum revealed evidence of the presence of C, N, O, Ru, and S elements (Fig. 2C). Additionally, the XPS spectra of IRD identified peaks at 164.88 eV, 284.80 eV, 287.28 eV, 397.11 eV, and 533.28 eV, corresponding to C-S, C-C, C = N/C = O, Metal-N bond, and hydroxyl groups in the IRD (Figure S3). To avoid interference from amorphous carbon, detailed spectra of Ru 3d were further examined, revealing two characteristic peaks at 281.73 eV and 284.69 eV (Ru 3d5/2, Ru 3d 3/2), attributed to Ru^{+} and Ru^{3+}, respectively, and a distinct satellite peak at 286.99 eV, demonstrating the formation of new Ru-S bonds (Fig. 2D). In addition, we examined the UV absorption spectra and observed that the absorption peak of ICG broadened in IRD and IRD@M. This is likely due to the coordination interaction, which alters the conjugated electron system of ICG, leading to an enhanced intramolecular and intermolecular charge transfer process and causing the homogeneous broadening of the absorption band. In contrast, the UV absorption spectra of IRD and IRD@M showed almost no significant difference, which indicates that the absorption peak primarily originates from the IRD core rather than the macrophage membrane (Figure S4).

These results suggest that the benzene ring from ICG likely serves as a coordination site for Ru^{3+}. Furthermore, Ru^{3+} interacts with the C-S bonds of DTPA, affecting their vibrational properties and forming coordination bonds with sulfur atoms, facilitating the dynamic self-assembly of Ru^{3+} with ICG and DTPA, thereby confirming the successful synthesis of IRD.

In vitro stability

Concerned about the poor photostability, ACQ phenomenon, and photodegradability of ICG. We explored the fluorescence changes of IRD and IRD@M within 120 h. As shown in the Fig. 2E-G, the fluorescence intensity of

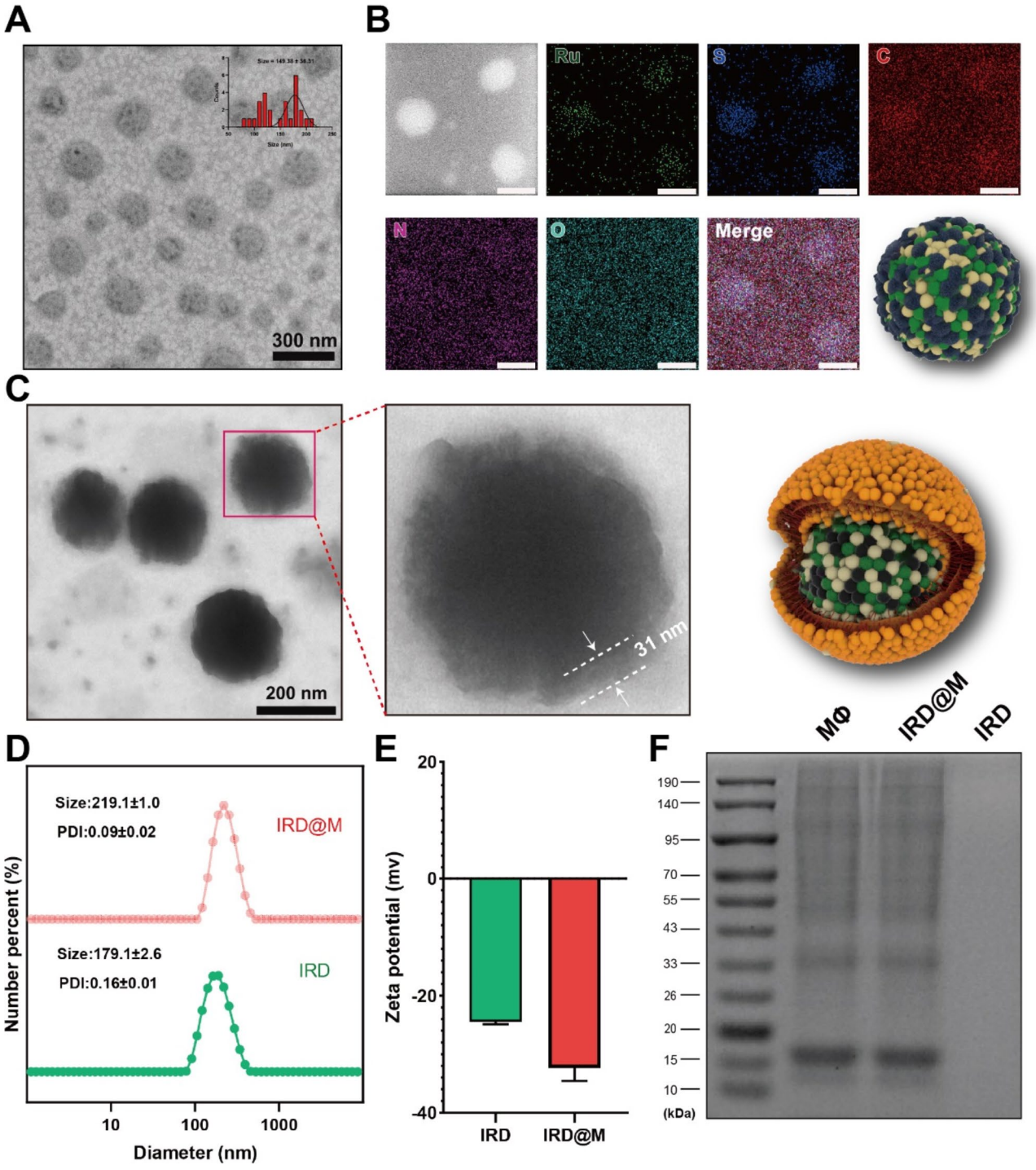

Fig. 1 Construction and characterization of IRD and IRDM. (**A**) TEM image of IRD. **B**) EDS elemental distribution map of IRD. Scale bar = 200 nm. (**C**) TEM image and its magnification of IRDM coated with macrophage membrane (Mø). (**D**) Hydrodynamic diameter and polydispersity index of IRD and IRD@M measured by DLS. (**E**) Zeta potential of IRD and IRD@M. (**F**) Protein profiles of Mø, IRD@M, and IRD detected by SDS-PAGE. Data are expressed as mean ± SD ($n = 3$)

ICG decreased dramatically after 120 h of incubation, in contrast, there was no obvious decreasing trend of IRD and IRD@M. It is worth mentioning that the IRD@M group appeared to have a slightly elevated fluorescence intensity compared to the very first one. The corresponding quantitative analysis showed that the fluorescence intensity of ICG gradually decreased within 120 h, while the fluorescence intensity of IRD and IRD@M exhibited

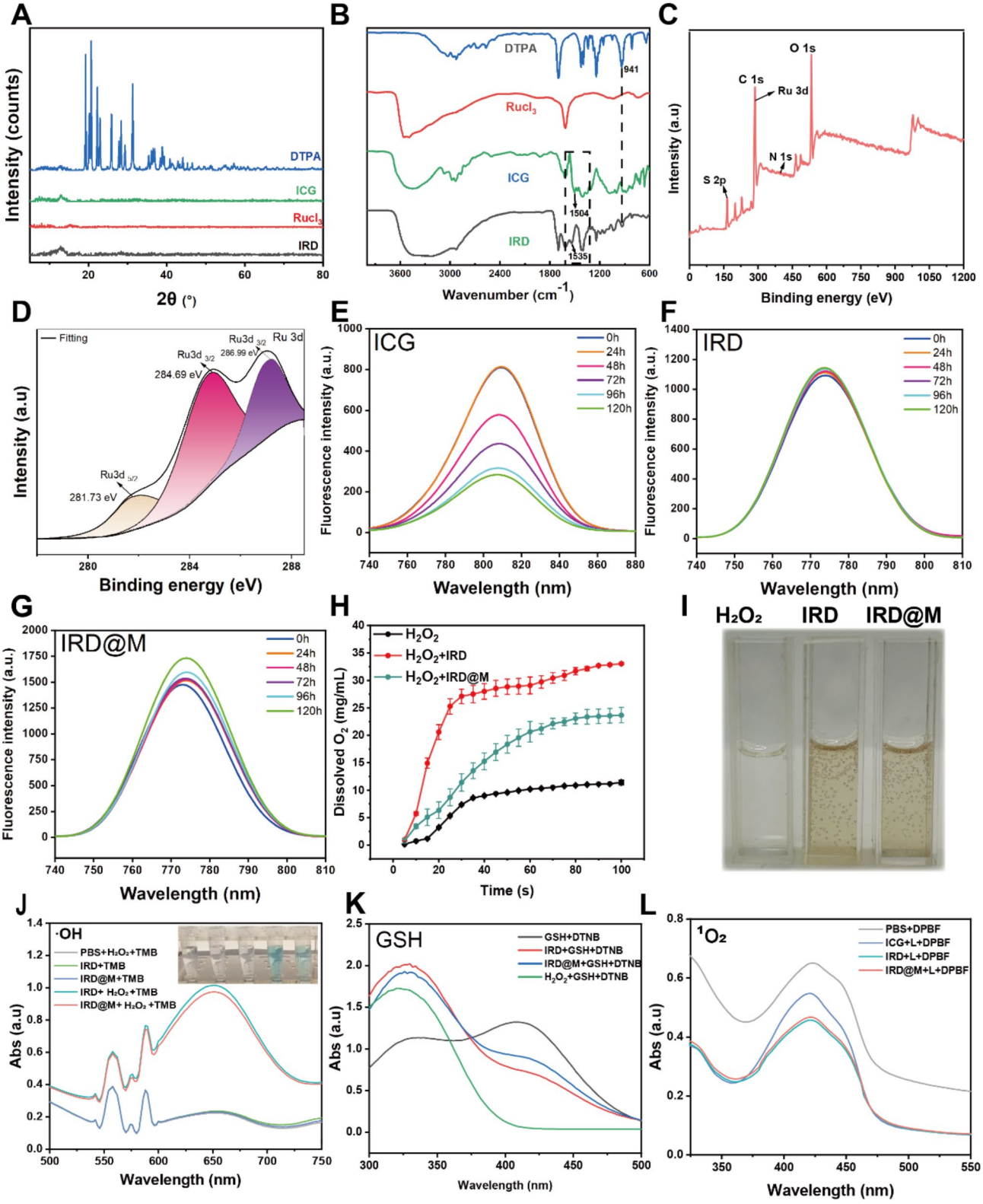

Fig. 2 Coordination mechanism, stability and catalytic properties of IRD. (**A**) XRD patterns of DTPA, ICG, $RuCl_3$ and IRD and (**B**) Fourier Transform Infrared Spectroscopy (FTIR). (**C**) XPS wide scanning pattern of IRD and (**D**) Ru3d spectrum. (**E**) Fluorescence spectra of ICG, (**F**) IRD and (**G**) IRD@M in water for 120 h. (**H**) Dissolved oxygen meter to detect the ability of IRD and IRD@M to catalyze the production of O_2 from H_2O_2 ($n = 3$). (**I**) White light photographs of the oxygen production of IRD and IRD@M. (**J**) TMB probe to detect the ability of IRD and IRD@M to react with H_2O_2 to produce ·OH. F(**L**) Determination of $^1O_2$ production after laser radiation (0.5 W, 5 min)

almost no significant decline (Figure S5).These experimental results indicate that the fluorescence stabilization of ICG was significantly improved, which may be attributed to the synergistic coordination between Ru^{3+} and ICG, while the phenomenon of elevated fluorescence intensity in the IRD@M group may be attributed to the rupture of the membrane leading to the release of ICG, which appeared to slightly increase the fluorescence intensity. Meanwhile, the improved fluorescence stability facilitates the maintenance of a longer excited-state lifetime, continuously transferring energy to oxygen molecules ($^3O_2$), thereby increasing the accumulation of $^1O_2$. Particle size stability is critical for the properties of nanomedicines. As shown in Figure S6, particle size of IRD in PBS exhibited significant variation, increasing from 180 nm to 300 nm over time, while no noticeable changes were observed for IRD@M. In addition, the optical image of IRD and IRD@M in PBS and serum-containing medium was observed, as shown in Figure S7, no aggregation of IRD and IRD@M was observed in the initial three days. It is worth mentioning that, on the fifth day, obvious aggregation and precipitation phenomenon was observed in the IRD group, whereas the IRD@M group remained good dispersion, which may be attributed to the fact that the PBS or the presence of higher ionic strength in the medium, which neutralized the charge on the surface of IRD, thus weakening the electrostatic repulsion and promoting aggregation and precipitation. But in the IRD@M group, the structural integrity of IRD was protected by possessing the protection of macrophage membranes, which in turn hindered the exchange of ions with the solution. Together, the above results demonstrate that the fluorescence photostability and physiological stability of ICG and nanoparticles can be greatly improved by the coordination of Ru^{3+} and the coating of macrophage membranes, which provides a solid foundation for our subsequent cell-animal experiments.

Assessment of O2, ROS recharge and GSH depletion in vitro

Due to the excellent CAT and POD activities of Ru, we subsequently explored their capability to generate O_2 and ·OH. Initially, high concentrations of H_2O_2 and IRD were mixed with IRD@M solution, O_2 content changes within 100 s were measured using a dissolved oxygen meter. As shown in Fig. 2H, the O_2 content significantly increased in both the IRD + H_2O_2 and IRD@M + H_2O_2 groups. Notably, the O_2 production capability of the IRD@M group was slightly lower than that of the IRD group. Additionally, optical images of oxygen production after mixing IRD and IRD@M with H_2O_2 revealed abundant bubbles in both IRD and IRD@M groups, indicating their CAT activity (Fig. 2I). The reduced oxygen production in the IRD@M group compared to IRD may be attributed to the protective effect of the membrane, which hinders complete reaction of Ru with H_2O_2, thereby attenuating oxygen production. Furthermore, the classic TMB oxidation method was employed to verify the POD activity of IRD and IRD@M. As depicted in Fig. 2J and Figure S8, this method was conducted under acidic conditions using TMB as the substrate. In the absence of H_2O_2, neither IRD nor IRD@M groups showed significant color reactions, and UV absorbance remained unchanged compared to the PBS group. Conversely, in the presence of H_2O_2, both IRD and IRD@M groups transitioned from colorless to blue, with a significant increase in UV absorbance at 652 nm. This indicates that ·OH generated by the reaction of IRD and IRD@M with H_2O_2 oxidized TMB to ox-TMB, confirming the POD activity of the materials. In addition, to further evaluate the catalytic efficiency of IRD@M, we measured the Michaelis-Menten kinetic parameters of CAT and POD enzyme activities. As shown in Figure S9, to determine the enzymatic kinetics of CAT, we measured the O_2 production rate by IRD@M over 100 s at different concentrations of H_2O_2 (6.25, 12.5, 25, 50, 100 mM). By fitting the relationship between reaction rate and substrate concentration using the Michaelis-Menten equation, the *Vmax* for CAT was calculated to be 0.1926 mg/s, and the *Km* was 33.34 mM. Additionally, we evaluated the effect of different concentrations of TMB (62.5, 125, 250, 500, 1000 μM) on the POD reaction rate, with a reaction time of 300 s. Using the same Michaelis-Menten equation fitting, the *Vmax* for POD was determined to be 1.785×10^{-8} M s^{-1}, and the *Km* was 201.3 μM. These results indicate that IRD@M exhibits good CAT and POD enzyme activities.

In recent years, nano-delivery strategies targeting GSH depletion based on disulfide bonds have garnered significant attention [35]. To investigate the ability of IRD and IRD@M to deplete GSH through disulfide bond interaction, DTNB, a reagent containing thiol groups, was used to react with the thiol groups (-SH) of GSH, producing a yellow product, TNB, which was employed to quantify the remaining GSH in the system. As shown in Fig. 2K, both the IRD and IRD@M groups exhibited a decrease in absorbance at 412 nm compared to the positive control (GSH + DTNB). This decrease can be attributed to the presence of DTPA in IRD and IRD@M, which contains disulfide bonds that readily react with the thiol groups in GSH, leading to a thiol-disulfide exchange reaction and the formation of new disulfide bonds, thereby converting reduced GSH to GSSG (oxidized glutathione) and consequently depleting GSH concentration. The slightly lower absorbance observed in IRD@M compared to IRD could be due to the membrane encapsulation reducing their exposure to the external environment, potentially limiting the oxidation of GSH by disulfide bonds. These

results demonstrate the effective GSH consumption capability of both IRD and IRD@M.

Further, enlightened by the strong O_2 rechargeability and the excellent fluorescence stability after coordination, we utilized the DPBF indicator to detect the yield of $^1O_2$ in IRD and IRD@M under laser irradiation. As shown in the Fig. 2L, it is interesting to note that IRD and IRD@M possessed a stronger $^1O_2$ production capacity at equal concentrations of ICG, which may be attributed to the larger Stokes shift of the formed substance after Ru^{3+} coordination, which helps to separate the wavelengths of excitation and emission light and reduces spectral "crosstalk" due to overlapping of luminescence. At the same time, the coordination environment constructed by Ru^{3+} can effectively gather the ACQ phenomenon, thus maintaining a high fluorescence conversion efficiency. Therefore, IRD and IRD@M can produce more $^1O_2$ under laser irradiation. In addition, we further investigated the release characteristics of IRD and IRD@M under different physiological environments. We found that in a simulated tumor microenvironment with high GSH levels (10 mM), the accumulation-release of ICG was maximized. Furthermore, in the presence of an acidic environment, the drug release was continuously enhanced (Figure S10). This provides a prerequisite for the subsequent safe and efficient killing of tumor cells both in vitro and in vivo.

Overall, the tumor microenvironment presents microacidic, hypoxic, high H_2O_2 levels and GSH. IRD and IRD@M can take full advantage of the high expression of H_2O_2 to generate O_2 and ·OH, and furthermore, under laser irradiation, they are able to increase the production of $^1O_2$, and more importantly, they are also able to consume GSH, which creates a solid platform for the potential of PDI to be realized.

In vitro cellular uptake and phototoxicity

The level of drug accumulation in the cell is a prerequisite for determining drug efficacy. Therefore, to investigate whether coating of macrophage membranes increases drug internalization, we incubated Hela cells with ICG, IRD, IRD@M for 1 h,4 h,8 h to assess the cellular uptake effect, respectively. The fluorescence intensity of ICG was used as a standard to assess the degree of cellular uptake. As shown in the Fig. 3A, it could be seen that the red fluorescence of all three groups was gradually enhanced with time, which proved that the uptake of ICG, IRD, IRD@M by HeLa cells was time-dependent. Notably, within each time point, IRD@M incubated HeLa cells possessed stronger fluorescence intensity in the cytoplasm compared to IRD and ICG groups. Meanwhile, the results of flow cytometry also consistent with these results (Fig. 3B), the IRD@M group showed stronger fluorescence signals at the same time intervals, and especially at 8 h, the uptake of IRD@M by HeLa cells was the strongest. The higher uptake of IRD compared to ICG may be attributed to coordination-induced formation of the IRD nanoparticle structure, which has a spherical morphology and a larger specific surface area. This enhances its affinity for the cell membrane, thereby facilitating the endocytosis of nanoparticles by cancer cells. In the case of IRD@M, the macrophage membrane coating likely increases receptor-mediated endocytosis, significantly improving cellular uptake. This provides a foundation for further investigations into the efficacy of nanomedicines both in vitro and in vivo.

The disruption of intracellular redox homeostasis triggered by ROS burst serves as a potent mechanism for inducing tumor cell death [36]. We next utilized the DCFH-DA probe, which can be oxidized by intracellular ROS to form 2',7'-dichlorodihydrofluorescein (DCF) and emit green fluorescence. This characteristic was utilized to further assess the levels of ROS within cells under different treatments. (Fig. 3C). When ICG, IRD, and IRD@M were incubated with HeLa cells without laser irradiation, no significant green fluorescence was observed. Once laser irradiation was applied, they exhibited varying degrees of green fluorescence compared to the control group, indicating that each laser treatment group could induce increased ROS production upon laser exposure. Furthermore, IRD and IRD@M groups displayed stronger green fluorescence under laser irradiation, possibly due to the POD activity of IRD and IRD@M, which catalyzes further production of ·OH within cancer cells and better generation of $^1O_2$ under laser irradiation, thereby triggering ROS burst. Remarkably, attributed to IRD@M enhanced internalization efficiency in cancer cells, excessive green fluorescence was observed particularly in the IRD@M + L group. Consistent results were further confirmed by flow cytometry (Fig. 3D), showing stronger fluorescence signals in cells treated with IRD@M + L compared to other groups. In addition, the corresponding flow cytometry-based fluorescence quantitative analysis also confirmed the same results, showing that the IRD@M + L group could effectively induce the generation of ROS (Figure S11). Therefore, these findings demonstrate the superior ability of the IRD@M group to stimulate ROS production under laser irradiation. Meanwhile, Overexpression of GSH can reduce oxidative stress, thereby mitigating apoptosis in cancer cells. Therefore, we utilized the GSH detection kit to investigate the effect of IRD@M on intracellular GSH levels. As shown in Figure S12, compared to the control group, the GSH content in HeLa cells decreased from 90 μM to 70.9 μM and 68 μM after incubation with IRD and IRD@M, respectively. This indicates that IRD and IRD@M effectively deplete GSH, which may help further enhance oxidative stress and promote cancer cell apoptosis. In addition, due to the excellent CAT enzyme activity

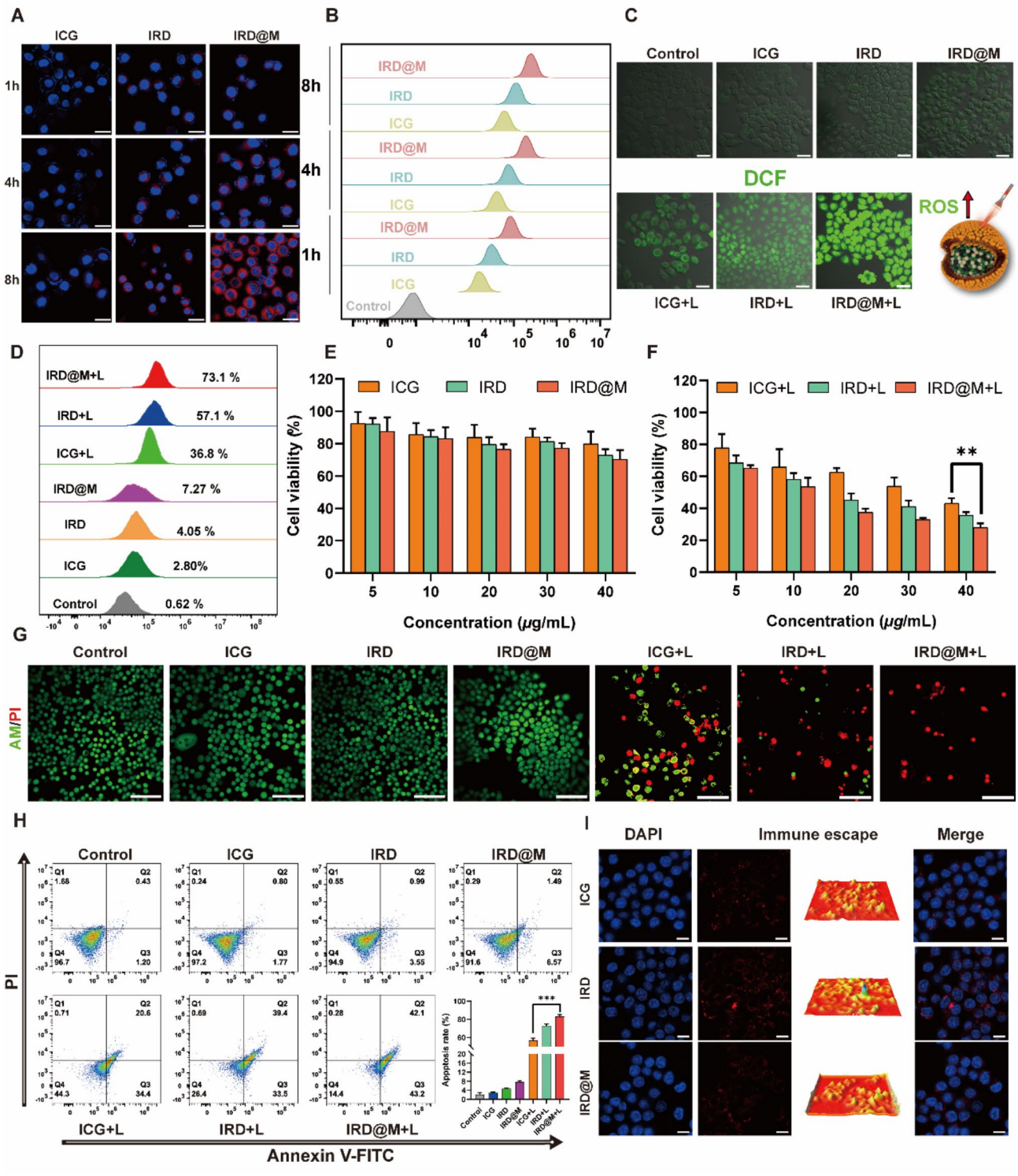

Fig. 3 IRD@M-mediated cellular uptake, oxidative stress, PDT efficacy, and immune escape. (**A**) CLSM images of Hela cells co-incubated with ICG, IRD, IRD@M for 1 h, 4 h, and 8 h, scale bar = 25 μm and (**B**) flow cytometry image. (**C**) CLSM images of Hela cells after co-incubation with ICG, IRD, IRD@M and ROS generation by laser radiation, scale bar = 50 μm and (**D**) flow cytometry images. Survival of Hela cells co-incubated by different groups (**E**) without laser(**F**)with laser irradiation. (**G**) CLSM images of live-dead staining, scale bar = 100 μm. (**H**) Apoptosis assay to detect apoptosis in Hela cells with laser or without laser by Annexin V/PI double labeling method after incubation with different groups. (**I**) Incubation of ICG, IRD, IRD@M to determine immune escape ability. Scale bar = 20 μm. Data are expressed as mean ± SD ($n = 3$). ** $p < 0.01$; and *** $p < 0.001$

of IRD@M, we further investigated the expression of HIF-1α in vitro by western blot. As shown in Figure S13, both the IRD and IRD@M groups were able to reduce the expression of HIF-1α in cells. This effect may be attributed to their CAT enzyme activity, which catalyzes the conversion of H_2O_2 to O_2 in tumor cells, thereby reducing the intracellular levels of HIF-1α. Notably, IRD@M exhibited a stronger ability to reduce HIF-1α expression, which may be due to its higher uptake by the cells.

Benefiting from the results of the ROS burst, we next evaluated the antitumor effect of IRD@M using the MTT assay. As shown in the Fig. 3E, after HeLa cells were incubated with each group of drugs for 24 h, the cell viability slightly decreased as the drug concentration increased, and immediately after, cells treated with different drug groups were irradiated with a 606 nm laser with a power of 1 W/cm^2 for 5 min, and both free and nanomedicine groups exhibited higher antitumor effects compared to the without laser. Additionally, the MTT assay results for TC-1 cells also showed corresponding outcomes, with the IRD@M + L group demonstrating the strongest cytotoxic effect, which may be attributed to the generation of $^1O_2$, ·OH, GSH depletion, and enhanced cellular uptake, ultimately resulting in synergistic damage to cancer cells (Figure S14). In addition, we further investigated the effect of different laser powers on the viability of Hela cells, as shown in Figure S15. The results demonstrated that, compared to the control group, the cell viability remained almost unchanged, indicating that laser powers below 2 W/cm² are non-toxic to the cells. Further, calcein-AM (green) and PI (red) were employed to label live and dead cells to further visualize the killing effect of IRD@M. As shown in the Fig. 3G, green fluorescence dominated the field of view when laser irradiation was not added, while red fluorescence became more and more prevalent in the laser group, showing a trend consistent with the MTT assay, and red fluorescence dominated in the IRD@M + L group, which was considered to be almost without the presence of live cells. In addition, the apoptosis assay was further used to quantitatively assess the anti-cancer effect of IRD@M. As shown in the Fig. 3H, the apoptosis rate in the IRD@M + L group was 85.3% (early apoptosis: 43.2%, late apoptosis: 42.1%), which was higher than that in the IRD + L group (72.9%) and the ICG + L group (55%), which exhibited the most effective tumor cell killing. Together, the above results illustrated that macrophage membranes could enhance the internalization of cancer cells, which triggered a powerful ROS storm through the catalytic ability of IRD, ultimately achieving efficient PDT.

As widely recognized, clearance by the mononuclear phagocyte system (MPS) poses a significant threat to nanomaterials upon entry into the body, with circulating phagocytes playing a crucial role. One of the primary strategies to evade MPS clearance is through biomimetic cell membrane camouflage. Therefore, we further investigated the uptake of nanodrugs by macrophages in vitro to simulate the clearance process in vivo. As shown in Fig. 3I, compared to the ICG group, the IRD group exhibited stronger red fluorescence, likely due to the superior physicochemical properties of the nanodrug. Specifically, the IRD@M group displayed weaker red fluorescence. Additionally, corresponding flow cytometry and fluorescence quantification analyses confirmed that the uptake of the nanodrug by macrophages in the IRD@M group was lower than that in the IRD group (Figure S16). This may be attributed to the macrophage membrane coating effectively shielding the nanodrug from recognition and clearance by the MPS, thereby enhancing its antitumor efficacy in subsequent in vivo experiments.

In vitro ICD effect

PDT-induced immunogenic cell death leads to the release of a large amount of DAMP, recruiting antigen-presenting cells and activating the host immune system to generate a cascade of immune responses that can target to kill tumor cells. Therefore, we investigated the translocation of CRT, the extracellular release of HMGB1, and ATP secretion in dying tumor cells following treatment. As the first molecular event of ICD, exposure of CRT on the surface of tumor cells binds to DC surface receptors and promotes its uptake by DCs [37]. As shown in Fig. 4A, exposure of CRT on the cell membrane exhibited distinct trends following treatment with different groups. The ICG + L group displayed weaker green fluorescence, whereas the IRD + L group showed higher green fluorescence. Moreover, HeLa cells treated with IRD@M + L exhibited intense green fluorescence, indicating significant expression of CRT protein on the cell membrane.

According to reports, the release of HMGB1 from the cell nucleus to the extracellular matrix is considered the second molecular event in ICD processes [38, 39]. It binds to the TLR4 receptor on DCs, promoting the processing and cross-presentation of tumor antigens by DCs [40]. As shown in Fig. 4B, immunofluorescence staining revealed that in the control group, HMGB1 was primarily localized in the cell nucleus. However, following laser treatment, a phenomenon was observed where green fluorescence shifted from the cell nucleus to the cell membrane or disappeared, indicating the translocation of HMGB1. What's more, in the IRD@M + L group, green fluorescence was nearly absent, suggesting extensive migration of HMGB1. Additionally, semi-quantitative analysis using Image J was performed on the immunofluorescence signals of CRT and HMGB1. The CRT results showed that the fluorescence intensity in the IRD + L group and IRD@M + L group was significantly higher compared to the ICG + L group. Notably, the IRD@M + L

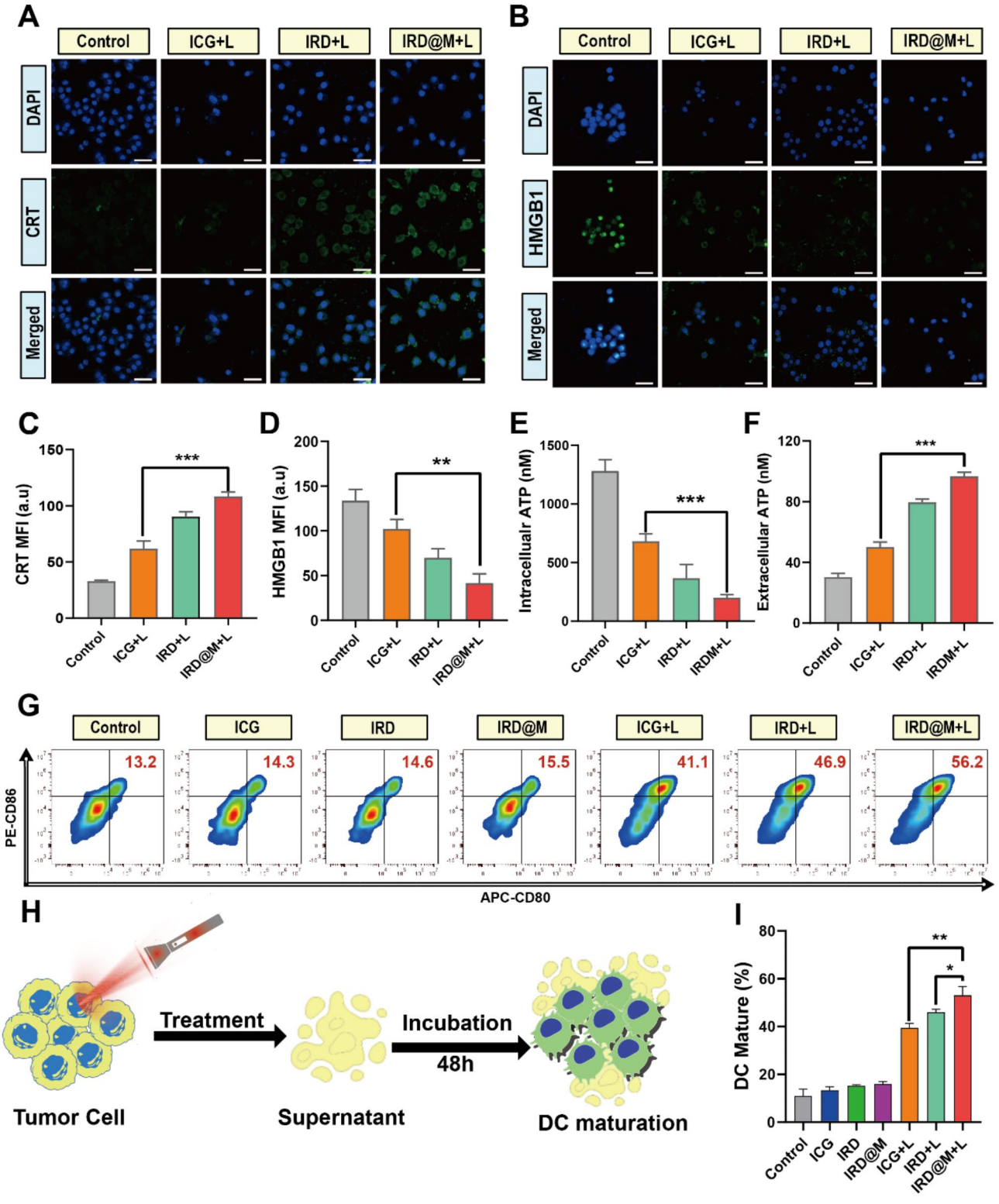

Fig. 4 In vitro ICD activation by IRD@M and promotion of DC maturation. (**A**) Immunofluorescence staining of CRT in Hela cells after different treatments, CLSM images, scale bar = 50 μm. (**B**) Immunofluorescence staining of HMGB1 in Hela cells after different treatments, CLSM images, scale bar = 50 μm. (**C**) MFI of CRT consistent with panel (**A**) (**D**) MFI of HMGB1 consistent with panel (B) (**E**) Intracellular ATP levels after treatment in various experimental groups. (**F**) Released ATP levels after treatment in various experimental groups. (**G**) Flow cytometric analysis of DC maturation after co-incubation with supernatants from different treated HeLa cells. (**H**) Schematic diagram of DC activation in vitro. (**I**) Quantitative analysis of corresponding DC maturation ($CD80^+$, $CD86^+$). Data are expressed as mean ± SD ($n = 3$). $^*P < 0.05$, $^{**}P < 0.01$, $^{***}P < 0.001$

group exhibited the strongest fluorescence intensity (Fig. 4C). In contrast, for HMGB1, the IRD@M + L group displayed the weakest green fluorescence (Fig. 4D).

The release of ATP serves as the third molecular event in the ICD process [41, 42]. It moves into autophagic vesicles via autophagy. Within these vesicles, Lysosomal Associated Membrane Protein 1 (LAMP1) facilitates lysosomal rupture, leading to ATP release. Subsequently, extracellular ATP from tumor cells binds to P2Y2 receptors on the surface of DCs, recruiting DCs to the tumor area [43]. Therefore, a luminescent ATP detection assay was utilized to quantify intracellular and extracellular ATP levels. As illustrated in Fig. 4E-F, following treatment with various drugs, intracellular ATP content gradually decreased while extracellular ATP levels increased. Notably, cells treated with IRD@M + L exhibited the lowest residual intracellular ATP content post-treatment, accompanied by the highest extracellular ATP release. These findings collectively underscore that, owing to the macrophage membrane's targeting capability and enhanced PDT effects, IRD@M + L induced CRT expression, facilitated HMGB1 translocation, and augmented ATP secretion, thereby effectively initiating the entire ICD process. This is expected to bolster dendritic cell maturation and subsequent cascade immune responses.

Based on enhanced ICD efficacy, we further investigated the maturation levels of dendritic cells (DCs) to assess whether IRD@M could enhance the immunogenicity of tumor cells. To simulate in vivo DC maturation, dendritic cells derived from C57 mouse bone marrow were co-cultured with supernatants from laser-treated HeLa tumor cells for 48 h (Fig. 4H). As shown in Fig. 4G, flow cytometry was used to assess the expression levels of co-stimulatory molecules ($CD80^+$, $CD86^+$) after co-incubation with tumor cell supernatants. Lower expression levels were observed before laser irradiation, indicating an inactive ICD process and immature DCs. Conversely, after laser irradiation, significant increases in CD80 and CD86 expression were noted. Moreover, the IRD@M + L group exhibited higher DC maturation proportions compared to the ICG + L and IRD + L groups, potentially due to its more effective induction of ICD, resulting in increased release of damage-associated factors that sensitize more DCs. Quantitative analysis of flow cytometry results showed that the IRD@M + L group induced a greater proportion of immature DCs to mature states (Fig. 4I). These results collectively demonstrate that IRD@M + L effectively activates the ICD process and promotes DC maturation.

In vivo biodistribution and hypoxia relief

Benefiting from the excellent biological properties of the membrane materials, we subsequently investigated the in vivo biodistribution of IRD@M in a TC-1 tumor-bearing mouse model. As shown in Fig. 5A, after intravenous administration, the green fluorescence at the tumor sites for both IRD and IRD@M increased over time, becoming brighter compared to the ICG group. This may be attributed to the enhanced permeability and retention (EPR) effect, which allows IRD and IRD@M to accumulate in the tumor tissue through the high permeability of tumor vasculature, whereas small molecule drugs tend to leak out. Additionally, the nanodrug can protect the core drug from early metabolism or clearance, thus enhancing its accumulation in the tumor region. Notably, IRD@M exhibited exceptionally strong green-yellow fluorescence at 12 h, with a slight decrease in fluorescence intensity at 24 h, indicating the highest tumor accumulation at 12 h, which may be attributed to the specific receptor recognition and affinity of the macrophage membrane that enables effective tumor targeting by the nanoparticles. Uniquely, fluorescence in metabolic organs was stronger in the ICG and IRD groups compared to IRD@M within 0.5–2 h post-injection. This could be attributed to the small molecules and nanoparticles being more readily recognized and intercepted by the liver and kidneys as foreign substances. In contrast, IRD@M, being encapsulated by macrophage membranes, appears to be treated as having a "pass" by the metabolic organs, leading to higher accumulation of the nano-drug at the tumor sites relative to other groups. Quantitative fluorescence data further demonstrated the high targeting efficiency of IRD@M towards the tumor sites (Fig. 5B). Additionally, fluorescence imaging of major tissues (heart, liver, spleen lung, kidney, tumor) was performed 24 h post-administration to accurately assess the targeting capability of IRD@M. As shown in Fig. 5C-D, IRD@M exhibited the strongest fluorescence intensity and green-yellow fluorescence at the tumor sites, highlighting its superior targeting ability. Meanwhile, both IRD and IRD@M showed partial accumulation in the liver and kidney, suggesting that they may undergo further metabolism in these organs (Figure S17). Therefore, it establishes a solid foundation for achieving better therapeutic outcomes in subsequent applications.

Tumor hypoxia is a significant challenge in PDT treatments, due to the vigorous metabolic demands of tumor cells and the abnormal vascular structure within tumors, HIF-1α is highly expressed on the surface of tumor cells. This hinders immune cell infiltration and compromises the efficacy of PDT [44, 45]. Due to the outstanding ability to recharge O_2 of IRD@M, we investigated whether IRD@M could alleviate the hypoxic tumor microenvironment and reduce the expression of HIF-1α. As shown in Fig. 5E, immunofluorescence was used to assess HIF-1α expression. It was observed that strong red fluorescence, indicating high HIF-1α expression, was present on the cell surface in the control and ICG groups. In

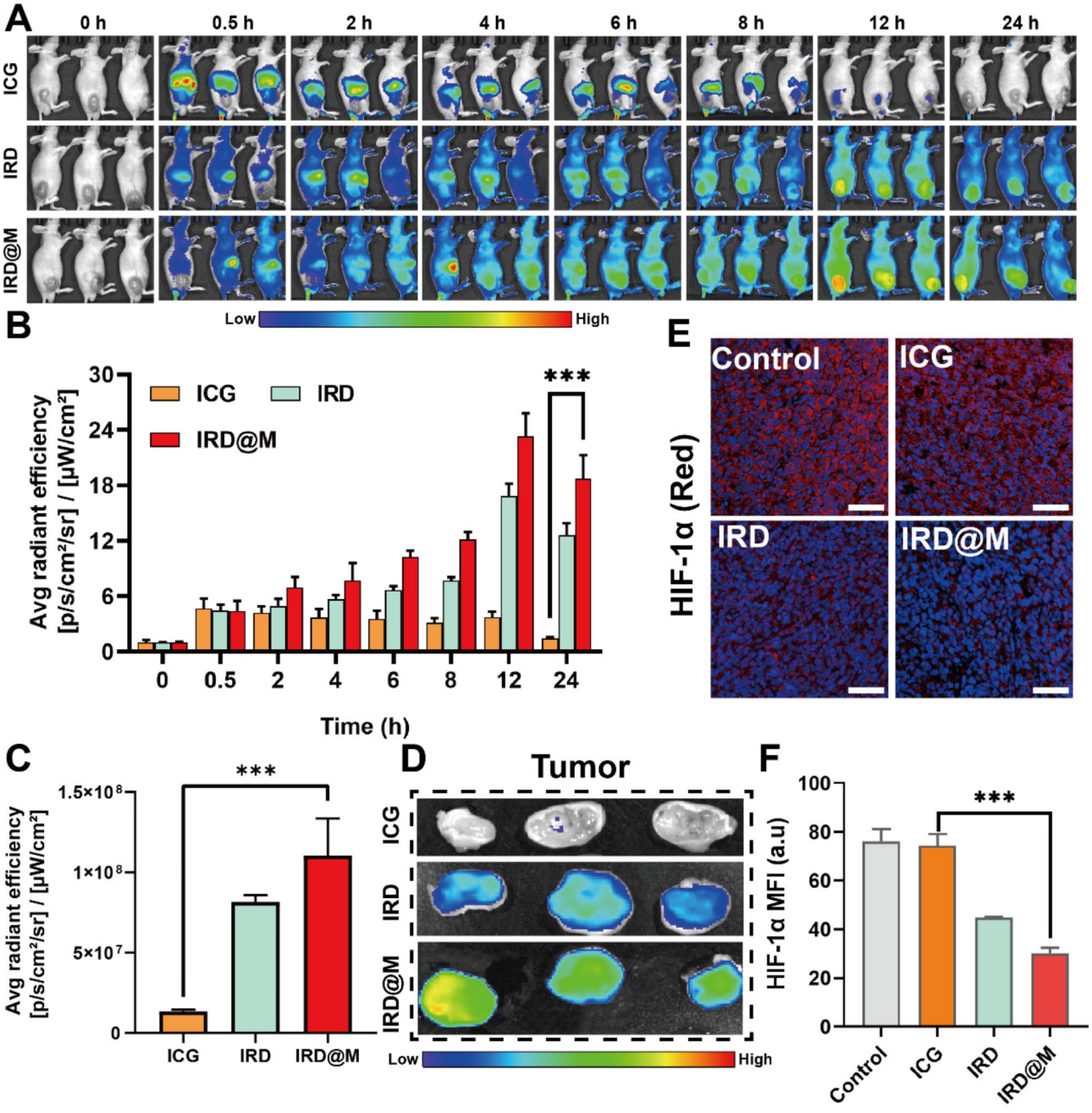

Fig. 5 In vivo fluorescence imaging and hypoxia attenuation. (**A**) Fluorescence imaging of mice at various time points within 24 h post-tail vein injection. (**B**) Quantification of fluorescence intensity at the corresponding tumor sites. (**C**) Fluorescence intensity of ex vivo tumor tissues 24 h post-administration. (**D**) Corresponding fluorescence images. (**E**) Hypoxia status of tumor tissues following treatment with different drug groups, scale bar = 50 μm. (**F**) Corresponding fluorescence trends. Data are expressed as mean ± SD ($n = 3$). *$P < 0.05$, **$P < 0.01$, ***$P < 0.001$

contrast, both the IRD and IRD@M groups exhibited significantly reduced red fluorescence. Particularly noteworthy, IRD@M markedly decreased the intensity of red fluorescence. Quantitative analysis confirmed IRD@M remarkable capability to alleviate tumor hypoxia, likely attributable to the excellent targeting effect of the macrophage membrane and effective oxygen-recharging capacity of IRD@M, leading to attenuation of the hypoxic tumor microenvironment (Fig. 5F).

In vivo antitumor efficacy and safety

Encouraged by the excellent tumor-targeting capability and mitigation of tumor hypoxia by IRD@M, we established a TC-1 tumor-bearing mouse model to evaluate the therapeutic effects of different drug groups. When

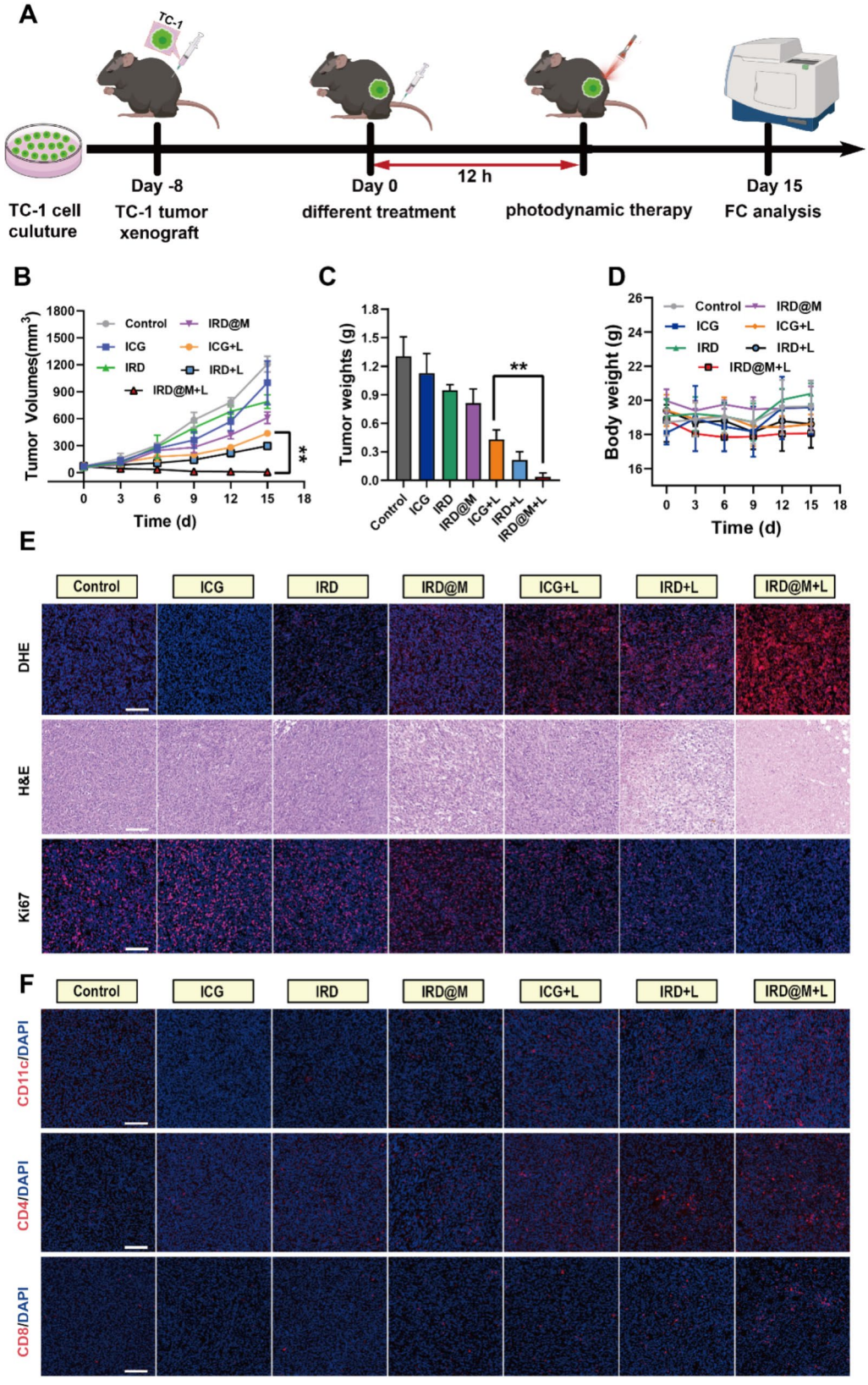

Fig. 6 (See legend on next page.)

(See figure on previous page.)

Fig. 6 In vivo tumor suppression mediated by IRD@M. (**A**) Schematic representation of the treatment regimen. (**B**) Growth curves of tumor volumes after treatment with different groups. (**C**) Average tumor volume at the end of treatment. (**D**) Body weight changes of mice throughout the entire treatment period. (**E**) Immunohistochemical staining of tumor sections after treatment with different groups using DHE, H&E, and Ki67 markers. Scale bar = 100 μm. (**F**) Immunohistochemical analysis of tumor tissues using CD11C, CD4, and CD8 antibodies. Scale bar = 100 μm. Data are presented as mean ± SD ($n = 5$). *$P < 0.05$, **$P < 0.01$, ***$P < 0.001$

tumor volumes reached 50–80 mm^3, mice were randomly divided into seven groups: (1) PBS, (2) ICG, (3) IRD, (4) IRD@M, (5) ICG + L, (6) IRD + L, (7) IRD@M + L. All laser groups received 606 nm laser irradiation (1 W/cm^2, 5 min) 12 h after intravenous drug administration (Fig. 6A). On day 0, all animals were injected via tail vein with different drug formulations (10 mg kg^{-1}). During the 15-day treatment period, mouse tumor volumes and body weights were measured regularly (every 3 days). Tumors in mice treated with ICG grew rapidly throughout the observation period with minimal growth inhibition (Fig. 6B). In comparison to the Control group, IRD and IRD@M exhibited signs of tumor growth suppression, likely due to their generation of ·OH and depletion of GSH leading to enhanced cellular oxidative stress and promotion of cell death. Furthermore, all laser groups showed significant antitumor effects, with the strongest observed in the IRD@M + L group. At the end of treatment, tumor weight measurements, ex vivo tumor imaging, and in vivo tumor images were consistent with trends in tumor volume changes, highlighting a pronounced antitumor effect in the IRD@M + L group compared to any other group (Figure S18-S19). Furthermore, as shown in Figure S20, the tumor inhibition rate in the laser-only group reached over 50%, while the ICG + L group achieved 63.8%, the IRD + L group reached 75.3%, and the IRD@M + L group exhibited a remarkable 99.3% inhibition. These results suggest that the IRD@M + L treatment significantly enhances tumor ablation, with no significant tumor tissue remaining after the treatment. Furthermore, there were no significant changes in mouse body weight throughout the treatment period (Fig. 6D), and no apparent pathological damage was observed in major tissues (Figure S21). Additionally, hemolysis assays evaluating blood compatibility showed less than 5% hemolysis for both IRD and IRD@M; notably, IRD@M demonstrated lower hemolysis levels compared to IRD (Figure S22). Therefore, the results indicate that IRD@M exhibits promising safety and efficacy in tumor therapy.

To further validate the enhanced therapeutic efficacy of IRD@M following initial PDT, ROS accumulation in tumor tissues was assessed using dihydroethidium (DHE) probe. As depicted in Fig. 6E, tumor tissues treated with IRD@M exhibited notable red fluorescence compared to the other three groups without laser irradiation, indicating increased ROS expression within tumor cells possibly due to the synergistic effects of macrophage membrane targeting capability and ·OH production. What's more, the IRD@M + L laser group displayed the highest ROS levels compared to other laser-treated groups, likely attributed to enhanced $^1O_2$ production by IRD, increased in situ oxygen concentration, ·OH contributed by CDT, and synergistic targeting capability of macrophage membranes, leading to a significant elevation in ROS within tumor tissues. Subsequently, tumor tissue damage was characterized from various perspectives. Hematoxylin and eosin (H&E) staining revealed that the Control and ICG groups exhibited neatly arranged and densely packed cells with regular morphology, whereas in the IRD@M + L treatment group, nuclear disappearance, cytoplasmic breakdown, nuclear membrane rupture, loose cell arrangement, and reduced density were observed. Furthermore, the lowest proportion of Ki67-immunopositive cells suggested that IRD@M + L treatment led to minimal proliferation of tumor cells.

In vivo cascade immune response

The immune efficacy provided by the PDT-activated ICD process and the recharging of in situ tumor oxygen from IRD@M provide a favorable environment for boosting the immune response. Therefore, we investigated whether such strategies could lead to increased infiltration of immune cells into tumor tissues. Dendritic cells (DCs) act as crucial mediators in the immune response, playing a pivotal role in the activation and differentiation of $CD4^+$ and $CD8^+$ T lymphocytes during cascade immune reactions. Hence, immunofluorescence staining of $CD11C^+$, $CD4^+$, and $CD8^+$ lymphocytes in tumor tissues was performed. As shown in Fig. 6F, the proportion of infiltrating $CD11C^+$ lymphocytes in tumor tissues was significantly higher in the IRD@M + L group, suggesting a greater recruitment of DCs in this group. Additionally, the red fluorescence intensity of $CD4^+$ and $CD8^+$ T cells was highest in the IRD@M + L group, indicating maximal T cell infiltration in this group. Following PDT treatment, extensive release of DAMPs from tumor sites and exposure of tumor antigens initiates the process of systemic cascade immune reactions. DCs in tumor-draining lymph nodes (TDLNs) capture DAMPs and present processed tumor-associated antigens to T cells, triggering immune responses. Subsequently, we examined the activation status of DCs and T cells in TDLNs using flow cytometry. As depicted in Fig. 7A-B, compared to the control group, the proportion of mature DCs ($CD11c^+CD80^+CD86^+$) significantly increased in the laser-treated group; notably, IRD@M + L treatment further enhanced DC maturation.

Concurrently, the proportion of T cells ($CD3^+CD8^+$) also increased, suggesting that IRD@M effectively activates DC maturation in TDLNs and cross-presents antigens to $CD8^+$ T cells, eliciting specific immune responses.

Upon stimulation with tumor antigens, immune cells in the spleen are activated and proliferate. Hence, the activation status of immune cells in spleen tissues was assessed using flow cytometry. As shown in Fig. 7C-D, the proportion of mature DCs and $CD4^+$ T cells significantly increased in the IRD@M + L group, indicating that IRD@M more effectively activates DCs and helper T cells in the spleen, which is crucial for tumor elimination. Collectively, these findings demonstrate that IRD@M effectively stimulates anti-tumor immune responses in the body, promoting increased infiltration of immune cells into tumor sites. This enhances the potential of PDT-induced immune responses, inflicting deeper damage on tumor cells.

Expression profile of tumor gene

To comprehensively elucidate the molecular mechanisms of IRD@M in anti-tumor action at the genetic level, RNA sequencing was conducted to evaluate potential differentially expressed genes (DEGs) and biological pathways between two systems (IRD@M + L and Control groups). DEGs were defined using a filter threshold of$|\log2FC|>1$ and FDR < 0.05. Heatmap analysis was employed to visually depict changes in gene expression levels post-PDT, revealing significant differential gene expression between the two groups, underscoring the efficacy of IRD@M phototherapy (Fig. 7E). Subsequently, the Kyoto Encyclopedia of Genes and Genomes (KEGG) database was utilized to decipher metabolic pathways potentially altered within cells post-PDT. As shown in Fig. 7F, upregulated genes were annotated to ten significantly enriched metabolic pathways, with notable activation observed in cytokine-cytokine receptor interaction and TNF signaling pathways, indicating strong correlation with activation of immune cells within tumor tissue. Additionally, a total of 424 DEGs were identified, with 222 downregulated genes and 202 upregulated genes represented by green and orange dots, respectively (Fig. 7G).Furthermore, gene ontology (GO) analysis was performed on differentially expressed genes post-IRD@M laser treatment, revealing significant enrichment in immune-related pathways, including lymphocyte-mediated immunity, immune response mediators, immunoglobulin immune response, B cell-mediated immunity, antigen binding, and other critical biological processes. These findings suggest that IRD@M significantly activates immune-related pathways and biological processes following PDT (Fig. 7H-I). Overall, IRD@M effectively promotes immune responses at tumor sites by laser, reversing the tumor immunosuppressive microenvironment and further enhancing anti-tumor immunity.

Conclusion

In summary, we have developed a ruthenium-based nanobattery coated with macrophage membranes, which not only exhibits excellent tumor targeting ability but also recharge O_2 at tumor sites, amplifies ROS, enhances PDT efficacy, and reverses the "immune desert" capability, achieving a more thorough eradication of tumor cells. This system catalyzes H_2O_2 to produce O_2 and ·OH, generating more $^1O_2$ under 606 nm laser irradiation compared to ICG components, while also depleting GSH. Additionally, the macrophage membrane coating enhances cancer cell uptake of nanodrugs, thereby improving therapeutic efficacy. Furthermore, in vitro experiments confirm its ability to amplify ROS and more effectively activate ICD processes. Moreover, following systemic administration, it selectively targets tumor sites, mitigates the tumor hypoxic microenvironment, reduces HIF-1α expression, and provides enhanced ROS efficiency upon NIR irradiation. This activation of in situ ICD processes triggers a cascade immune response, synergizing with in situ O_2 charging to accumulate more infiltrating immune cells and induce specific damage to tumor cells. In conclusion, this straightforward and efficient system further unleashes the potential of PDT, enhancing its stimulation of anti-tumor immune responses to complementarily synergize with tumor damage.

Experimental section

Materials

Ruthenium trichloride ($RuCl_3$) was purchased from Shanghai Bide Pharmaceutical Technology Co., Ltd. ICG was obtained from Shanghai Hao Yun Chemical Technology Co., Ltd. Shanghai Hao Yun Chemical Technology. 3-(4,5-dimethylthiazol-2)-2,5-diphenyltetrazolium bromide (MTT), 3,3',5,5'-tetramethylbenzidine (TMB) was purchased from Shanghai Yuanye Biotechnology Co., Ltd.1,3-diphenylisobenzofuran (DPBF) was purchased from Shanghai Aladdin Biochemical Technology Co., Ltd. Dithiobispropionic acid (DTPA), 5,5'-dithiobis(2-nitrobenzoic acid) (DTNB) was purchased from Shanghai Macklin Biochemical Co., Ltd. 4′,6-diamidino-2-phenylindole (DAPI), Hochest33258, 2',7'-Dichlorodihydrofluorescein diacetate (DCFH-DA), Annexin V-FITC/PI Staining Kit, ATP Detection Kit were purchased from Beyotime Institute of Biotechnology Co., Ltd. Anti-CRT was sourced from Santa Cruz Biotechnology (Shanghai) Co., Ltd. Anti-HMGB1, FITC Goat Anti-Rabbit IgG (H + L) was purchased from Wuhan Aibotec Biotechnology Co. Ltd. Antibodies specific for CD86, CD80, CD11c,

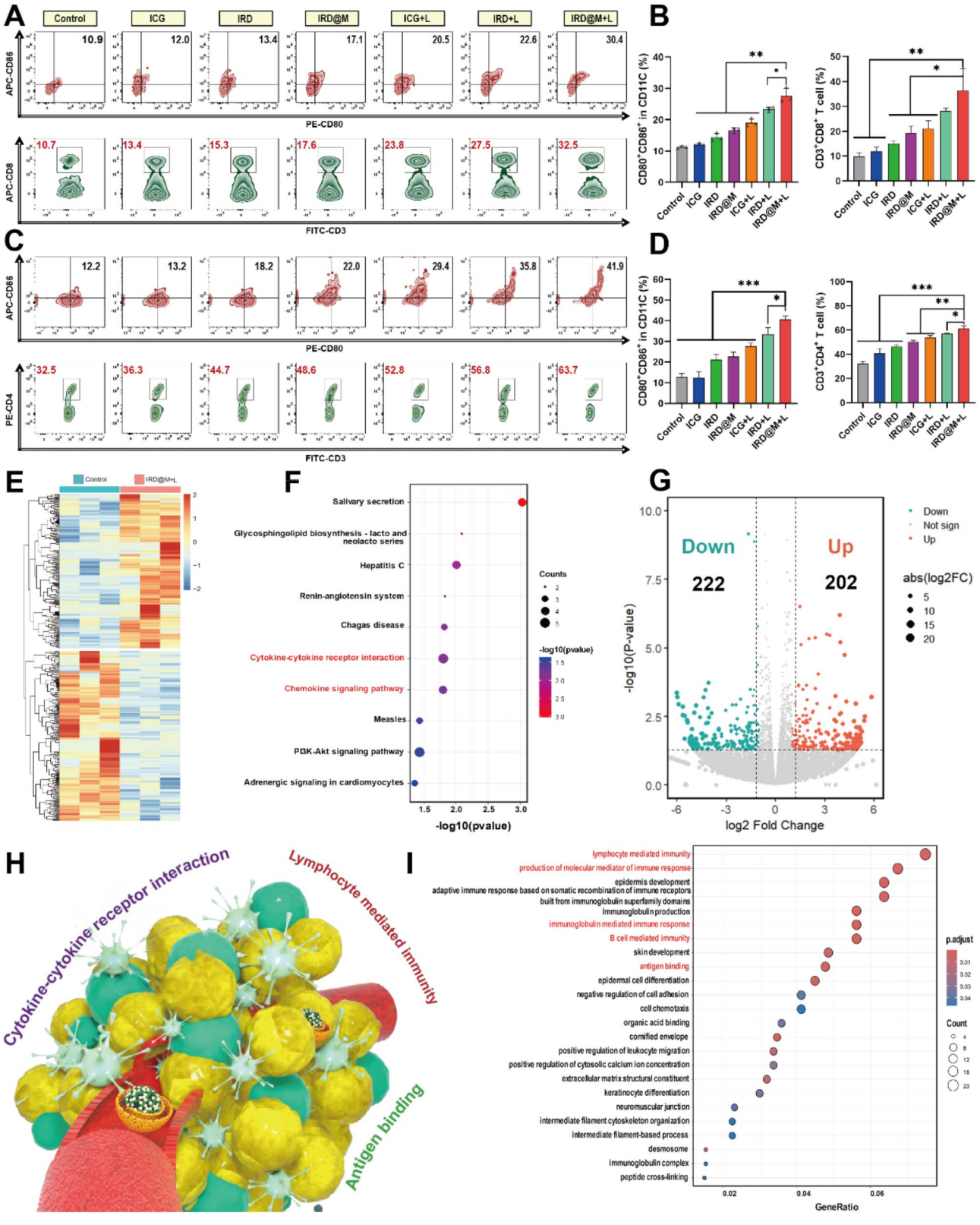

Fig. 7 (See legend on next page.)

(See figure on previous page.)

Fig. 7 Mechanisms of in vivo antitumor immune responses. **A**) Flow cytometric analysis of DC maturation ($CD80^+CD86^+$ in CD11C) and T cell activation ($CD3^+CD8^+$) in tumor-draining lymph nodes after different treatments. **B**) Quantitative analysis of DC maturation ($CD80^+CD86^+$ in CD11C) and T cell activation ($CD3^+CD8^+$). **C**) Flow cytometric analysis of DC maturation ($CD80^+CD86^+$ in CD11C) and T cell activation status ($CD3^+CD4^+$) in spleens after different treatments. **D**) Quantitative analysis of DC maturation ($CD80^+CD86^+$ in CD11C) and T cell activation ($CD3^+CD8^+$). **E**) Heatmap showing differentially expressed genes (DEGs) between the control group and IRD@M + L treated group. **F**) KEGG pathway enrichment analysis of DEGs mediated by IRD@M + L (showing top 10 upregulated pathways). **G**) Volcano plot of DEGs between the IRD@M + L group and control group. **H**) Schematic representation of immune response mechanisms at the tumor site. **I**) Gene Ontology (GO) classification of biological processes for DEGs mediated by IRD@M + L (showing top 25 pathways). Thresholds for differential analysis:|log2FC| > 1 and FDR < 0.05. Results are presented as mean ± SD ($n = 3$). *$P < 0.05$, **$P < 0.01$, ***$P < 0.001$

CD4, CD8, and CD3 were procured from BD Biosciences for use in this study.

Instrument

The nano sizes and zeta potentials of IRD and IRD@M were measured using a Malvern Laser Particle Size Zeta Potential Analyzer (Zetasizer Nano ZS90, UK). The morphology of IRD and IRD@M was observed using Transmission Electron Microscopy (TEM, JEOL JEM 2100 F). Fourier Transform Infrared Spectroscopy (FTIR, VERTEX 70, Germany), X-ray Photoelectron Spectroscopy (XPS, Escalab 250XI, Germany), and X-ray Diffraction (XRD, D8 advance, Germany) were employed to acquire the corresponding spectral data. Fluorescence stability was assessed by obtaining spectral images with a fluorescence spectrophotometer (Luster Light, F97Pro, China). The ultraviolet absorption and fluorescence values at specific wavelengths were determined using a multifunctional microplate reader (Molecular Devices, SpectraMax Id5, USA). Confocal Laser Scanning Microscopy (Nikon, AIR HD25, Japan) was utilized to obtain CLSM images. In vivo fluorescence distribution images were captured using a small animal imaging system (PerkinElmer, Lumina XRM5, USA). Immune and apoptosis outcomes were detected by flow cytometry (Beckman Coulter, CytoFLEX, USA).

Cell line and mice

Hela, TC-1, and RAW264.7 cells were kept in liquid nitrogen tanks in the group. 6-8-week-old female C57BL/6 mice were purchased from the First Affiliated Hospital of Xinjiang Medical University, and kept in temperature-controlled chambers with free access to food and water. All animal experiments were conducted in strict accordance with a protocol approved by the Institutional Animal Care and Use Committee of Xinjiang University.

Bioinformatics analysis

Transcriptome data were processed by R software (R-4.3.3), the mouse whole genome annotation package was "org.Mm.eg.db", and the thresholds for analysis of differences were|log2FC|>1 and FDR < 0.05.

Construction of IRD

Typically, 1 mL of DTPA methanol solution (1 mg/mL) was mixed with an equal amount of ICG (1 mg/mL) methanol solution, and then 1 mL of $RuCl_3$ methanol solution (1 mg/mL) was added drop by drop. After being stirred for 3 h, 1 mL of deionized water was added until appearance of a heating phenomenon on the surface of the tube wall, and then the stirring was continued for 3 h. The methanol was removed by vacuum rotary evaporation using a rotary evaporator (CCA-1112 A, Shanghai Ailang, China). Finally, the crude product was washed by three centrifugations (10,000 rpm, 10 min, and 4 °C) and dispersion cycles to obtain IRD. In this synthesis process, the ratio, the order of addition, and the choice of solvent are critical factors for obtaining nanoparticles with uniform morphology.

Extraction of macrophage membranes

The macrophage membranes were derived from the RAW264.7 cell line. Specifically, cell membranes were extracted using low-permeability ultrasonic fragmentation and gradient centrifugation, as previously described [46]. Briefly, macrophages were collected and placed in hypotonic lysate for 24 h. The ice-bath ultrasonic fragmentation was performed with the associated parameters (Power: 200 W, Ultrasonic Interval: 5 s, and Time: 10 min). The resulting homogenate was centrifuged at 4 °C and 2000 rpm for 10 min. After that, the resulting supernatant was centrifuged at 4 °C and 20,000 rpm for 30 min. The resulting precipitate was washed with deionized water. In order to obtain the macrophage membranes of uniform size, aqueous filter membranes with pore sizes of 800 nm and 450 nm were extruded three times each, respectively, and then stored at -80 °C in PBS for the following experiments.

Construction of IRD@M

The extracted macrophage membranes were thoroughly mixed with IRD solution on a shaker at 37 °C and 220 rpm for 2 h. and then sonicated by an ultrasound machine at 100 W for 150 s. The precipitate was collected by centrifugation in PBS and stored at 4 °C for the following experiments.

In vitro fluorescence stability

In vitro fluorescence stability of IRD and IRD@M was evaluated by fluorescence spectroscopy, and the same concentration of ICG was used as the control group (20

μg/mL). The fluorescence spectra of IRD and IRD@M were measured every 24 h for 5 days.

In vitro O2 generation assay

In vitro O_2 generation of IRD and IRD@M was assessed by a dissolved oxygen meter. In brief, three groups including H_2O_2, IRD + H_2O_2, and IRD@M + H_2O_2 were established, in which the concentration of H_2O_2 was 1 mM, and the concentrations of IRD and IRD@M were 100 μg/mL. After that, three groups were added into 5 mL of small beaker and then stirred at 200 rpm. Finally, the amount of O_2 generation was determined within 100 s by a dissolved oxygen meter (JPBJ-608, Shang hai Leici, China).

OH radical detection

TMB was employed to detect the production of hydroxyl radicals. The subgroups are as follows: (1) PBS + H_2O_2 + TMB, (2) IRD + TMB, (3) IRD@M + TMB, (4) IRD + H_2O_2 + TMB, (5) IRD@M + H_2O_2 + TMB, in which the concentration of H_2O_2 was 100 μM/mL, the concentration of TMB was 0.1mM/mL, and the concentration of IRD and IRD@M drugs were both 100 μg/mL, were added to the solution of pH = 5. The solution was incubated at room temperature for 10 min, the color change was observed and the absorbance at 652 nm was detected by UV spectrophotometer (UV-4802 S, Shanghai Unocal Corporation, China).

Michaelis-Menten kinetic parameters of IRD@M

CAT enzyme activity

To determine the CAT activity of IRD@M, different concentrations of H_2O_2 (6.25, 12.5, 25, 50, 100 mM) were prepared. 40 μg/mL of IRD@M was added to test tubes containing H_2O_2 (pH = 7.4). The O_2 produced within 100 s was measured using a dissolved oxygen meter, and the reaction rate was recorded.

POD enzyme activity

To assess the POD enzyme activity, different concentrations of TMB (62.5, 125, 250, 500, 1000 μM) were prepared. 40 μg/mL of IRD@M was added to test tubes containing TMB (pH = 5), followed by the addition of 1 mM H_2O_2. The reaction was allowed to proceed for 300 s. The kinetic parameters were calculated by plotting data according to the Michaelis-Menten Eq.

$$V_0 = \frac{V_{max}[S]}{K_m + [S]} \quad (1)$$

In vitro 1O2 determination

DPBF was used to specifically detect $^1O_2$ production. Setting up the grouping: (1) PBS + DPBF, (2) ICG + L + DPBF, (3) IRD + L + DPBF, (4) IRD@M + L + DPBF, the concentration of ICG was all set at 20ug/mL, and the concentration of DPBF was 10μm/mL, and the laser groups were all irradiated using a 660 nm laser (0.5 W//cm^2) for 5 min, followed by detection of the 422 nm by UV spectrophotometer (UV-4802 S, Shanghai Unocal Corporation, China).

Measurement of GSH depletion

DTNB was used to determine the GSH depletion. Briefly, four groups including GSH + DTNB, GSH + IRD + DTNB, GSH + IRD@M + DTNB, and H_2O_2 + GSH + DTNB were designed. The associated concentrations in IRD and IRD@M, GSH, and DTNB were 100 μg/mL, 10 mM, and 10 mM. After co-incubation for 12 h, all solutions from four groups were filtered through aqueous filter membranes with pore sizes of 220 nm, and 30 μL of DTNB solution was added. Next, after incubation for 30 min. Next, the absorbance value of four groups was measured by UV spectrophotometer (UV-4802 S, Shanghai Unocal Corporation, China) at 412 nm.

In vitro drug release

In vitro drug release of IRD and IRD@M was evaluated using a dialysis method. Briefly, 1 mL of IRD solution and IRD@M solution were placed in dialysis bags (molecular weight cutoff of 3500 Da) and immersed in 49 mL of 1 × PBS with different conditions (pH 7.4, pH 5.0, and 10 mM GSH). At predetermined time points (0, 0.5, 1, 4, 8, 12, 24 h), 1 mL of the solution outside the dialysis bag was withdrawn, followed by the addition of 1 mL of fresh PBS. The cumulative drug release of ICG was then calculated based on the volume of liquid collected at each time point.

In vitro cellular uptake

Hela cells were seeded at a density of 1.5×10^5 cells per well in a 12-well plate and cultured for 24 h. After that, cells were treated with free ICG, IRD, and IRD@M at equivalent ICG (10 μg/mL) concentration at 37 °C for 1, 4, and 8 h hours. For quantitative analysis of the cellular uptake, cells were collected via trypsinization and centrifugation at 1000 rpm for 10 min). Next, the suspension was removed, and then cells were washed thrice with PBS. Ultimately, the intracellular fluorescence intensity was determined by flow cytometer (Beckman Coulter, CytoFLEX, USA) after filtration through a aqueous filter membranes with pore sizes of 100 μm.

For qualitative analysis of the cellular uptake, cells were washed thrice with PBS, fixed in 4% paraformaldehyde solution for 15 min, and counterstained with Hoechst 33,342 for 10 min. Afterward, cells were observed by CLSM (Nikon, AIR HD25, Japan).

In vitro viability

The MTT method was used to detect the viability of ICG, IRD, and IRD@M. In detail, Hela cells were seeded in 96-well cell culture plates at a density of 1×10^4 cells/well and then incubated at 37 °C for 24 h. After that, the cells were treated with different concentrations of ICG, IRD, and IRD@M. Following incubation for 8 h, cells were irradiated with a 660 laser (1 W/cm^2) for 5 min, and then continuously incubated for 12 h. Afterward, MTT was added and then incubated for 4 hours. Next, after adding DMSO solution and shaking evenly, the excessive MTT solution was removed by centrifugation (1200 rpm for 7 min). Finally, the absorbance value of cells treated with all the above groups at 490 nm was detected by an enzyme marker (Molecular Devices, SpectraMax Id5, USA).

In vitro apoptosis

Flow cytometric analysis was conducted to estimate the rate of apoptotic cells, HeLa cells were employed. In detail, cells within the log-growth phase were counted by a cytometer and then diluted to a density of 1.5×10^5 cells/mL. Afterward, 2 mL of cell suspension was added to each well within a 12-well plate. After overnight incubation within an incubator at 5% CO_2 and 37 °C, the culture medium was removed. Subsequently, these cells were washed thrice with PBS. Next, 1 mL of fresh culture medium and 1 mL of ICG, IRD, and IRD@M (40 μg/mL) were added, respectively. Next, cells were irradiated with a 660 nm laser (1 W/cm^2) for 5 min and then cultured for 24 h. Cells were further collected and then stained by an Annexin V/PI apoptosis detection kit. Finally, in order to quantify the percentage of apoptotic cells, the collected results were analyzed via flow cytometry (Beckman Coulter, CytoFLEX, USA) and then analyzed with FlowJo 7.6 software (FlowJo, Ashland, OR, USA).

Next, the calcein-AM/PI assay was used to assess cell viability and mortality. Logarithmically growing HeLa cells (1.5×10^5 cells/mL) were seeded in confocal dishes and cultured for 24 h. After removing the culture medium, fresh medium containing ICG, IRD, or IRD@M (40 μg/mL) was added, and the cells were incubated for 8 h. Subsequently, cells were irradiated with a 660 nm laser (1 W/cm²) for 5 min, followed by another 24-hour incubation. Finally, cells were incubated in dark with calcein-AM/PI staining solution for 20 min. Cell viability and death were observed using confocal laser scanning microscopy (CLSM, Nikon AIR HD25, Japan).

Detection of intracellular ROS accumulation

Hela cells were inoculated into 12-well plates and confocal dishes at a density of 1.5×10^5 cells/well and incubated overnight. After treating the cells with different drug groups (ICG + L, IRD + L, and IRD@M + L) for 8 h, the cells were incubated with DCFH-DA for 25 min at 37 °C. Then, the cells were exposed to laser irradiation for 5 min (1 W/cm^2) and the intracellular ROS were quantified by flow cytometry (Beckman Coulter, CytoFLEX, USA). To show the intracellular ROS accumulation, the cells were washed, then observed by CLSM (Nikon, AIR HD25, Japan).

Depletion of GSH at the cellular level

Intracellular GSH levels were assessed using a GSH assay kit. HeLa cells were seeded at 5×10^5 cells per well in a 6-well plate. Cells were treated with different drugs at a concentration of 40 μg/mL for 48 h. Subsequently, wash with PBS, collect the cells, and rapidly freeze and thaw in liquid nitrogen. The absorbance was measured by multifunctional microplate reader (Molecular Devices, SpectraMax Id5, USA) at 412 nm.

In vitro immune evasion assay

To evaluate the ability of the drug to evade the immune system, RAW264.7 cells were used as a model to assess the extent of drug uptake in vitro. Logarithmically growing RAW264.7 cells (1.5×10^5 cells/mL) were seeded in confocal dishes and incubated for 24 h. After removing the culture medium, fresh medium containing ICG, IRD, or IRD@M (with ICG concentration standardized to 10 μg/mL) was added and co-incubated for 8 h. Subsequently, the medium was discarded, and the cells were washed three times with PBS. The fluorescence intensity of ICG was observed using confocal laser scanning microscopy (CLSM), with excitation at 675 nm and emission at 695 nm.

Assay of ICD-related biomarker

The evaluation of ICD was mainly determined by the migration of CRT from the inside out, the external secretion of HMGB1, and the release of ATP. Hela cells were incubated with ICG, IRD, and IRD@M for 8 h, and then exposed to laser (1 W/cm^2) irradiation for 5 min, and then continued to be incubated for another 24 h, and then the cells were washed by PBS. were incubated with anti-mouse CRT and HMGB1 primary antibody at 4 °C for 12 h, and then incubated with FITC-coupled secondary antibody for 2 hours, and then the intracellular fluorescence was observed by CLSM (Nikon, AIR HD25, Japan). For the detection of intracellular ATP, the cells were processed as described above, and then the intracellular ATP was detected in accordance with the instructions for the use of the ATP kit.

In vitro DC maturation assay

Bone marrow cells were extracted from tibia and femur of 6–8 weeks old C57BL/6 mice, after alcohol sterilization and washing with PBS solution, the cells were

cultured in complete medium containing GM-CSF until day 7 to obtain the induced cultured DCs. Subsequently, the induced cultured DCs were co-cultured with supernatants obtained from nanomedicine-treated Hela cells for 48 h. The expression levels of surface co-stimulatory molecules CD80 and CD86 were detected by flow cytometry (Beckman Coulter, CytoFLEX, USA).

In vivo tumor targeting effect

To study the targeting effect of IRD@M, ICG, IRD, IRD@M was injected into TC-1 hormonal mice, which were used for NIR fluorescence imaging studies. Drug accumulation was monitored using an in vivo imaging system at predetermined time points. Subsequently, the primary tissues and tumor samples were harvested for ex vivo fluorescence imaging.

Examination of in vivo tumor hypoxia Attenuation

The unilateral TC-1 subcutaneous tumor model was used, and when the tumor became hard and the volume was about 200 mm^3, the tumor-bearing mice were randomly divided into four groups: (1) Control; (2) ICG; (3) IRD; and (4) IRD@M. After the administration of the drug via tail vein for 12 h, the mice were euthanized to isolate the tumors. The tumor sections were then subjected to HIF-1α immunofluorescent staining to assess the improvement in hypoxia.

Antitumor efficacy in vivo

To establish the tumor model, TC-1 cells (1.5×10^6 cells/mouse) were subcutaneously inoculated. Tumor size and body weight of mice were recorded every 3 days. Tumor volume was calculated using the formula: tumor volume = (length × width^2) × 0.5. When tumors reached approximately 50–80 mm^3 in volume, mice were randomly divided into 7 groups ($n = 5$ per group). Tumor-bearing mice were then injected with PBS, ICG, IRD, IRD@M, and ICG, IRD, IRD@M plus laser radiation (660 nm, 5 min, 1 W/cm^2), all at a dose of 10 mg/kg. Tumor size and body weight were monitored every 3 days post-injection. After 15 days, mice were euthanized, tumors were harvested, washed with PBS, fixed in 4% paraformaldehyde, and subsequently processed for histopathological analysis.

Examination of anti-tumor immune response in mice

At the end of the treatment course, anti-tumor immune response in mice was assessed by flow cytometry (Beckman Coulter, CytoFLEX, USA). Typically, after mice were executed, spleen and tumor-draining lymph nodes were collected and processed into single-cell suspensions. To detect DC maturation, the treated single-cell suspensions were stained with anti-mouse FITC-CD11C, APC-CD86, PE-CD80 antibodies. To detect classical T cells, cell suspensions were stained with anti-mouse FITC-CD3, APC-CD8, PE-CD4.

Statistical analysis

Data were analyzed using Graph Pad Prism (Version 8.0), R software (Version 4.3.3), and data were expressed as the mean ± SD of at least three repeated measurements. t-tests (two-sided)) were performed to analyze the data. $p < 0.05$ was considered statistically significant. * $p < 0.05$, ** $p < 0.01$, and *** $p < 0.001$.

Supplementary Information

The online version contains supplementary material available at https://doi.org/10.1186/s12951-025-03255-8.

Supplementary Material 1

Acknowledgements

Not applicable.

Author contributions

Guoyu Xia: Writing-original draft, Data curation. Zhongxiong Fan: Conceptualization, Writing-original draft, Supervision, Funding acquisition. Qingluo Wang: Data curation. Jianmin Li: Data curation. Yuxiang Zhang: Data curation. Adila Aipire: Data curation Qiurong Su: Data curation. Ying Li: Supervision, Funding acquisition. Zhenqing Hou: Writing-original draft, Supervision. Jinyao Li: Writing-original draft, Supervision, Funding acquisition.

Funding

This work was supported by grants from the Key Research and Development Program in the Xinjiang Uygur Autonomous Region (2023B02030, 2023B02030-1).

Data availability

No datasets were generated or analysed during the current study.

Declarations

Ethics approval and consent to participate

All animal experiments were conducted in accordance with the guidelines of the Ethics Committee of Xinjiang University, and the experiments were approved by the Ethics Committee of Xinjiang University (XJUAE-2023-023).

Consent for publication

All authors agree for publication.

Competing interests

The authors declare no competing interests.

Author details

[1]School of Pharmaceutical Sciences, Institute of Materia Medica, Xinjiang University, Urumqi 830017, China
[2]Xinjiang Key Laboratory of Biological Resources and Genetic Engineering, College of Life Science and Technology, Xinjiang University, Urumqi 830017, China
[3]Xiamen Key Laboratory of Traditional Chinese Bio-Engineering, Xiamen Medical College, Xiamen 361023, China
[4]College of Materials, Xiamen University, Xiamen 361005, China
[5]Xinjiang Medical University, Affiliated Hospital 6, Urumqi 830002, China

Received: 22 November 2024 / Accepted: 19 February 2025
Published online: 04 March 2025

References

1. Shen L, Zhou T, Fan Y, Chang X, Wang Y, Sun J, et al. Recent progress in tumor photodynamic immunotherapy. Chin Chem Lett. 2020;31:1709–16.
2. Li Y, Xie J, Um W, You DG, Kwon S, Zhang L, et al. Sono/Photodynamic Nanomedicine-Elicited Cancer immunotherapy. Adv Funct Mater. 2021;31:2008061.
3. Gao Y, Wang Z, Jin X, Wang X, Tao Y, Huang S et al. Enhanced osteosarcoma immunotherapy via $CaCO_3$ nanoparticles: remodeling tumor acidic and immune microenvironment for photodynamic therapy. Adv Healthc Mater. 2024;2400538.
4. Tian L, Li X, Guo L, Huang L, Wu X, Gao W. Visualized photodynamic nanomaterials activating tumor-associated immune landscape as a next-generation anticancer strategy. Coord Chem Rev. 2024;517:216027.
5. Chen X, Yong Z, Xiong Y, Yang H, Xu C, Wang X, et al. Hydroxyethyl starch conjugates co-assembled nanoparticles promote photodynamic therapy and antitumor immunity by inhibiting antioxidant systems. Asian J Pharm Sci. 2024;19:100950.
6. Huang J, Liu X, Lin M, Xiao Z, Shuai X. Light-inducible nanodrug-mediated photodynamic and anti-apoptotic synergy for enhanced immunotherapy in triple-negative breast cancer. Biomater Sci. 2024;12:2639–47.
7. Lebelo MT, Joubert AM, Visagie MH. Warburg effect and its role in tumourigenesis. Arch Pharm Res. 2019;42:833–47.
8. Deng X, Shao Z, Zhao Y. Solutions to the drawbacks of photothermal and photodynamic Cancer therapy. Adv Sci. 2021;8:2002504.
9. Zhao H, Xu J, Wang Y, Sun C, Bao L, Zhao Y, et al. A photosensitizer discretely loaded nanoaggregate with robust photodynamic effect for local treatment triggers systemic antitumor responses. ACS Nano. 2022;16:3070–80.
10. Wang P, Wang X-Y, Man C-F, Gong D-D, Fan Y. Advances in hyperbaric oxygen to promote immunotherapy through modulation of the tumor microenvironment. Front Oncol. 2023;13:1200619.
11. Malla R, Kumari S, Ganji SP, Srilatha M, Nellipudi HR, Nagaraju GP. Reactive oxygen species of tumor microenvironment: Harnessing for Immunogenic cell death. Biochimica et biophysica acta (BBA) - Reviews on Cancer. 2024;1879:189154.
12. Guan R, Xie L, Rees TW, Ji L, Chao H. Metal complexes for mitochondrial bioimaging. J Inorg Biochem. 2020;204:110985.
13. Gupta G, Kumari P, Ryu JY, Lee J, Mobin SM, Lee CY. Mitochondrial localization of highly fluorescent and photostable BODIPY-Based Ruthenium(II), Rhodium(III), and Iridium(III) metal complexes. Inorg Chem. 2019;58:8587–95.
14. Hu W, He T, Zhao H, Tao H, Chen R, Jin L, et al. Stimuli-Responsive reversible switching of intersystem crossing in pure organic material for smart photodynamic therapy. Angew Chem Int Ed. 2019;58:11105–11.
15. Wen K, Tan H, Peng Q, Chen H, Ma H, Wang L, et al. Achieving efficient NIR-II Type-I photosensitizers for photodynamic/photothermal therapy upon regulating chalcogen elements. Adv Mater. 2022;34:2108146.
16. Zhou X, Shi C, Long S, Yao Q, Ma H, Chen K, et al. Highly efficient photosensitizers with molecular vibrational torsion for Cancer photodynamic therapy. ACS Cent Sci. 2023;9:1679–91.
17. Ren Q, Wang H, Li D, Dao A, Luo J, Wang D, et al. An Electron Donor–Acceptor structured Rhenium(I) complex Photo-Sensitizer evokes mutually reinforcing Closed-Loop ferroptosis and immunotherapy. Adv Healthc Mater. 2024;13:2304067.
18. Liu C, Li M, Li P, Bai Y, Pang J, Fan L, et al. Ruthenium (II)-Coordinated supramolecular metallodrug complex realizing oxygen Self-Supply in situ for overcoming hypoxic tumors. Adv Funct Mater. 2021;31:2105837.
19. Cong C, Li C, Cao G, Liu C, Yuan Y, Zhang X, et al. Dual-activity nanozyme to initiate tandem catalysis for doubly enhancing ATP-depletion anti-tumor therapy. Biomaterials Adv. 2022;143:213181.
20. Xia F, Hu X, Zhang B, Wang X, Guan Y, Lin P, et al. Ultrasmall ruthenium nanoparticles with boosted antioxidant activity upregulate regulatory T cells for highly efficient liver injury therapy. Small. 2022;18:2201558.
21. Liu J, Shi L, Wang Y, Li M, Zhou C, Zhang L, et al. Ruthenium-based metal-organic framework with reactive oxygen and nitrogen species scavenging activities for alleviating inflammation diseases. Nano Today. 2022;47:101627.
22. Chen X, Yang Y, Ye G, Liu S, Liu J. Chiral ruthenium nanozymes with Self-Cascade reaction driven the NO generation induced macrophage M1 polarization realizing the lung Cancer cocktail therapy. Small. 2023;19:2207823.
23. Eda S, Nasibullin I, Vong K, Kudo N, Yoshida M, Kurbangalieva A, et al. 28.Biocompatibility and therapeutic potential of glycosylated albumin artificial metalloenzymes. Nat Catal. 2019;2:780–92.
24. Yang Z-C, Gu Q-S, Chao J-J, Tan F-Y, Mao G-J, Hu L, et al. Glutathione-activated biotin-targeted dual-modal imaging probe with improved PDT/PTT synergistic therapy. Anal Chim Acta. 2024;1316:342860.
25. Tang S, Li G, Zhang H, Bao Y, Wu X, Yan R, et al. Organic disulfide-modified folate carbon Dots for tumor-targeted synergistic chemodynamic/photodynamic therapy. Biomater Sci. 2023;11:3128–43.
26. Zhu Y, Yu F, Tan Y, Wen L, Li Y, Yuan H, et al. Guiding appropriate timing of laser irradiation by polymeric micelles for maximizing Chemo-Photodynamic therapy. IJN. 2020;15:6531–43.
27. Zeng Y, Gu Q, Li D, Li A, Liu R, Liang J, et al. Immunocyte membrane-derived biomimetic nano-drug delivery system: a pioneering platform for tumour immunotherapy. Acta Pharmacol Sin. 2024;45(12):2455–73.
28. Gao Y, Zhou R, Wang Q, Qi S, Lv Y, Liu S, et al. Natural killer cell membrane doped supramolecular nanoplatform with immuno-modulatory functions for immuno-enhanced tumor phototherapy. Chin Chem Lett. 2024;35:109521.
29. Shan T, Wang W, Fan M, Bi J, He T, Sun Y, et al. Effective glioblastoma immune sonodynamic treatment mediated by macrophage cell membrane cloaked biomimetic nanomedicines. J Controlled Release. 2024;370:866–78.
30. Shen T, Yang S, Qu X, Chen Z, Zeng L, Sun X, et al. A bionic Trojan horse-like gene delivery system hybridized with tumor and macrophage cell membrane for cancer therapy. J Controlled Release. 2023;358:204–18.
31. Lopes J, Lopes D, Pereira-Silva M, Peixoto D, Veiga F, Hamblin MR, et al. Macrophage cell Membrane-Cloaked nanoplatforms for biomedical applications. Small Methods. 2022;6:2200289.
32. Wang C, Li C, Zhang R, Huang L. Macrophage membrane-coated nanoparticles for the treatment of infectious diseases. Biomed Mater. 2024;19:042003.
33. Wu Y, Wan S, Yang S, Hu H, Zhang C, Lai J, et al. Macrophage cell membrane-based nanoparticles: a new promising biomimetic platform for targeted delivery and treatment. J Nanobiotechnol. 2022;20:542.
34. Liu Y, Qi Y, Chen C, Jin Y, Du S, Qiao J, et al. Platelet-mimetic nano-sensor for combating postoperative recurrence and wound infection of triple-negative breast cancer. J Controlled Release. 2023;362:396–408.
35. Ma W, Wang X, Zhang D, Mu X. Research progress of disulfide bond based tumor microenvironment targeted drug delivery system. International Journal of Nanomedicine.
36. Wen S, Zhang W, Yang J, Zhou Z, Xiang Q, Dong H. Ternary Bi_2WO_6 /TiO_2–Pt heterojunction sonosensitizers for boosting sonodynamic therapy. ACS Nano. 2024;18:23672–83.
37. Janssens S, Rennen S, Agostinis P. Decoding Immunogenic cell death from a dendritic cell perspective. Immunol Rev. 2024;321:350–70.
38. Mishchenko T, Mitroshina E, Balalaeva I, Krysko O, Vedunova M, Krysko DV. An emerging role for nanomaterials in increasing immunogenicity of cancer cell death. Biochim Et Biophys Acta (BBA) - Reviews Cancer. 2019;1871:99–108.
39. Li D, Liu S, Ma Y, Liu S, Liu Y, Ding J. Biomaterials that induce Immunogenic cell death. Small Methods. 2023;7:2300204.
40. Qi H, Li Y, Geng Y, Wan X, Cai X. Nanoparticle-mediated Immunogenic cell death for cancer immunotherapy. Int J Pharm. 2024;656:124045.
41. Galluzzi L, Vitale I, Warren S, Adjemian S, Agostinis P, Martinez AB, et al. Consensus guidelines for the definition, detection and interpretation of Immunogenic cell death. J Immunother Cancer. 2020;8:e000337.
42. Pan H, Liu P, Zhao L, Pan Y, Mao M, Kroemer G, et al. Immunogenic cell stress and death in the treatment of cancer. Semin Cell Dev Biol. 2024;156:11–21.
43. Kroemer G, Galassi C, Zitvogel L, Galluzzi L. Immunogenic cell stress and death. Nat Immunol. 2022;23:487–500.
44. Ma J, Al Moussawi K, Lou H, Chan HF, Wang Y, Chadwick J, et al. Deficiency of factor-inhibiting HIF creates a tumor-promoting immune microenvironment. Proc Natl Acad Sci USA. 2024;121:e2309957121.
45. Wang Y, Huo J, Li S, Huang R, Fan D, Cheng H, et al. Self-Rectifiable and Hypoxia-Assisted Chemo-Photodynamic nanoinhibitor for synergistic Cancer therapy. ACS Appl Mater Interfaces. 2022;14:10092–101.
46. Jiang Y, Nie D, Hu Z, Zhang C, Chang L, Li Y et al. Macrophage-Derived nanosponges adsorb cytokines and modulate macrophage polarization for renal cell carcinoma immunotherapy. Adv Healthc Mater. 2024;2400303.

Publisher's note